



A new analysis of experimental data on olivine rheology

Jun Korenaga¹ and Shun-Ichiro Karato¹

Received 6 April 2007; revised 21 September 2007; accepted 23 October 2007; published 14 February 2008.

[1] We present a new statistical framework to analyze rock deformation data and determine a corresponding flow law and its uncertainty. All experimental uncertainties, including inter-run bias, are taken into account in the new formalism. Our approach is based on Bayesian statistics and is implemented by a Markov chain Monte Carlo method. We apply this approach to published data on the subsolidus deformation of synthetic olivine aggregates and try to establish experimental constraints on the rheology of Earth's upper mantle. Deformation data are interpreted on the basis of a composite flow law, which includes diffusion and dislocation creep mechanisms under both dry and wet conditions. We show that olivine rheology under wet conditions suffers major uncertainties suggesting the influence of poorly characterized parameters such as water content during deformation. Also, the pressure dependence of creep is still poorly constrained because of the lack of high-quality data under high pressures. However, our statistical analysis provides a solid framework to obtain a permissible range of flow laws constrained by the existing data, which will help geodynamic modeling with well-defined statistical bounds.

Citation: Korenaga, J., and S.-I. Karato (2008), A new analysis of experimental data on olivine rheology, *J. Geophys. Res.*, *113*, B02403, doi:10.1029/2007JB005100.

1. Introduction

[2] The constitutive relation between stress and strain rate for silicate minerals controls how the crust and mantle respond to applied forces. In particular, the constitutive relation for olivine is usually believed to govern the rheology of Earth's upper mantle because olivine is the most abundant phase (with a volume fraction of $\sim 60\%$) and also the weakest in most cases [e.g., Karato and Wu, 1993]. Because of this significance in mantle dynamics, the rheological properties of forsteritic olivine have been studied extensively in the past to derive its dependence on temperature, pressure, stress, grain size, and composition [e.g., Weertman, 1970; Goetze and Evans, 1979; Chopra and Paterson, 1984; Karato et al., 1986; Bai et al., 1991; Hirth and Kohlstedt, 1995a; Mei and Kohlstedt, 2000a; Karato and Jung, 2003]. Though mantle rheology can also be inferred from geophysical observations such as postglacial rebound [e.g., Wu and Peltier, 1983; Nakada and Lambeck, 1989] and the geoid [e.g., Hager et al., 1985; Ricard and Wuming, 1991], this observational approach is limited to estimating average viscosity with low spatial resolution. For a number of geodynamical problems, we need more than average viscosity, and laboratory experiments on rock deformation provide essential constraints on how the mantle may actually deform under various temperature and pressure conditions.

[3] Owing to experimental efforts in the past two decades or so, we now have a detailed understanding of olivine rheology both in diffusion and dislocation creep regimes [e.g., Hirth and Kohlstedt, 2003]. Along with this maturity in experimental studies, the numerical modeling of mantle dynamics has become progressively sophisticated by incorporating various complexities in mantle rheology [e.g., Braun et al., 2000; Hall and Parmentier, 2003; Billen and Hirth, 2005; Kneller et al., 2005]. Such elaboration on numerical models would result in more realistic predictions, without which it would be difficult to interpret geophysical observations in terms of subsurface dynamics. Seismic anisotropy, for example, is often used to infer mantle flow pattern because the dislocation creep of olivine results in the development of lattice-preferred orientation. Dislocation creep, however, takes place only when deviatoric stress exceeds some critical value, below which diffusion creep predominates, and this critical stress is known to depend on temperature, pressure, grain size, and water content. Connecting mantle flow and seismic anisotropy thus requires modeling with composite rheology, which deals with this delicate competition between different creep mechanisms.

[4] Deformation experiments can provide direct constraints on these details of creep mechanisms, but strain rates attained in laboratories are usually on the order of 10^{-5} s^{-1} , which is ten orders of magnitude faster than geological strain rates ($\sim 10^{-15} \text{ s}^{-1}$). This discrepancy in strain rates is unavoidable because deformation experiments must be done on a timescale of hours. To enhance strain rates, grain sizes are reduced to microns and deviatoric stresses are increased to $\sim 100 \text{ MPa}$, whereas the grain size of mantle olivine is typically on the order of millimeters [e.g., Ave Lallemand et al., 1980] and deviatoric stresses are

¹Department of Geology and Geophysics, Yale University, New Haven, Connecticut, USA.

expected to be on the order of 1 MPa in most of the mantle [e.g., *Hager and O'Connell*, 1981]. The temperature range that can be explored is also narrow (~ 200 K); strain rates would be too small to be measured at lower temperatures, and samples would melt at higher temperatures. Considerable extrapolation is thus involved when using experimentally derived mantle rheology in numerical modeling. Because nontrivial uncertainties are usually associated with such experimental constraints, it is important to know how such uncertainties affect our inference based on geodynamical models.

[5] The uncertainty of olivine rheology, however, has not been fully described. As shown in the next section, the functionality of olivine rheology is complex, involving at least 18 parameters. Though previous studies often report the uncertainty of some of those parameters such as activation energy [e.g., *Hirth and Kohlstedt*, 2003], an error analysis would be incomplete without specifying how it is correlated with the uncertainty of other parameters. Moreover, parameter estimation itself does not seem to be so reliable in previous studies. To estimate activation energy, for example, experimental data are usually normalized to constant grain size and constant stress, for which grain-size and stress exponents need to be specified. Estimated activation energy and its uncertainty depend not only on normalized data but also on the uncertainty of these exponents, but the influence of the latter is rarely taken into account in the literature on olivine rheology. It is possible to estimate all of relevant parameters simultaneously by nonlinear inversion, but earlier attempts are incomplete especially in terms of handling experimental uncertainties [e.g., *Parrish and Gangi*, 1981; *Sotin and Poirier*, 1984]. *Sotin and Poirier* [1984], for example, applied the nonlinear inversion method of *Tarantola and Valette* [1982b] for the deformation of sodium chloride, and their approach has been used for other minerals as well [e.g., *Poirier et al.*, 1990; *Franssen*, 1994; *Renner et al.*, 2001]. This inversion method, however, is implemented by an iterative procedure similar to Newton's root-finding algorithm, and thus a solution may not be unique and iteration may not converge if nonlinearity is too severe. Such difficulty is expected when estimating a composite flow law (e.g., diffusion and dislocation creep combined), and stably inverting for all of relevant parameters may not be possible [e.g., *Bystricky and Mackwell*, 2001]. Furthermore, the theory behind it requires that a priori constraints on flow-law parameters must follow the Gaussian distribution, and even if this condition is met, the uncertainty of parameters (i.e., their a posteriori covariance) cannot be correctly estimated because most of experimental uncertainties (other than uncertainty in strain rates) have to be neglected in the linear approximation adopted by the theory [*Tarantola and Valette*, 1982b, section 2.5].

[6] The purpose of this paper is to present a more flexible statistical framework to analyze rock deformation data and determine a corresponding flow law and its uncertainty. We apply this new approach to published data on the deformation of olivine aggregates and establish experimental bounds on upper mantle rheology. Our approach is based on Bayesian statistics and is implemented by a Markov chain Monte Carlo (MCMC) method. These concepts are explained in some details in the next section on theoretical formulation. The compilation of experimental data is then

described, and the statistical representation of olivine rheology is derived by a series of MCMC simulations. We also briefly discuss the implications of this newly derived rheology. Our theoretical formulation in the following uses olivine rheology as an example, but its overall strategy should also be applicable to other minerals with minor tuning if needed.

2. Theoretical Formulation

2.1. Flow Law

[7] We consider two deformation mechanisms, power law dislocation creep and diffusion creep, under a range of water content. The previous studies suggested that the flow-law parameters are different between water-saturated ("wet") and water-poor ("dry") conditions [e.g., *Mei and Kohlstedt*, 2000a, 2000b]. The difference in flow-law parameters between these two different conditions is likely due to the difference in relevant defects involved in each regime [e.g., *Karato*, 2007, Chap. 20]. Therefore we assume the following four different flow laws:

$$\dot{\epsilon}_{\text{diff,dry}} = A_1 d^{-p_1} \sigma \exp\left(-\frac{E_1 + pV_1}{RT}\right), \quad (1)$$

$$\dot{\epsilon}_{\text{diff,wet}} = A_2 d^{-p_2} C_{OH}^{r_2} \sigma \exp\left(-\frac{E_2 + pV_2}{RT}\right), \quad (2)$$

$$\dot{\epsilon}_{\text{dis,dry}} = A_3 \sigma^{n_3} \exp\left(-\frac{E_3 + pV_3}{RT}\right), \quad (3)$$

$$\dot{\epsilon}_{\text{dis,wet}} = A_4 C_{OH}^{r_4} \sigma^{n_4} \exp\left(-\frac{E_4 + pV_4}{RT}\right), \quad (4)$$

where $\dot{\epsilon}$ is a strain rate, the subscripts 'diff' and 'dis' denote diffusion creep and dislocation creep, respectively, and the subscripts 'dry' and 'wet' denote dry and wet conditions, respectively. The symbol $\dot{\epsilon}_{\text{diff,dry}}$, for example, represents a strain rate due to diffusion creep under a dry condition. A_i 's are scaling constants, d is average grain size in microns, σ is deviatoric stress in MPa, C_{OH} is water content in ppm H/Si, E_i 's are activation energies, p is pressure, V_i 's are activation volumes, R is the universal gas constant, and T is absolute temperature. There are three kinds of exponents to describe dependency on grain size (p_1 and p_2), stress (n_3 and n_4), and water content (r_2 and r_4). We assume linear rheology for diffusion creep so that the stress exponent is unity for $\dot{\epsilon}_{\text{diff,dry}}$ and $\dot{\epsilon}_{\text{diff,wet}}$, and no dependency on grain size for dislocation creep. The total number of flow-law parameters is thus 18. We do not consider the Peierls mechanism [e.g., *Goetze and Evans*, 1979], which becomes important for low temperature and high stress, nor grain boundary sliding [e.g., *Hirth and Kohlstedt*, 2003], which depends on both grain size and stress. The effect of the Peierls mechanism should be marginal at most for experimental data considered in this study, given their limited temperature and stress ranges. *Hirth and Kohlstedt* [2003] suggested that grain boundary sliding may be important at conditions near the

transition from diffusion to dislocation creep, but it is not clear whether grain boundary sliding can be an important, *rate-limiting* process at such conditions. Strong experimental support for grain boundary sliding may be found for other minerals such as ice [e.g., *Goldsby and Kohlstedt*, 1997, 2001], but for olivine, the demonstration of *Hirth and Kohlstedt* [2003] hinges primarily on the accuracy of diffusion creep flow law they assumed (see their Figure 7a). As we will show in this study, existing experimental data can be explained well by a simple combination of diffusion and dislocation creep, leaving little room for grain boundary sliding.

[8] Note that we use single measures of strain rate and stress to characterize a flow law. This is a simplification in which plastic isotropy is assumed. Both strain rate and stress are second-rank tensors, and a general constitutive relation between them requires a fourth-rank tensor for viscosity. However, conducting deformation experiments with different deformation geometries is highly complicated, and a scalar constitutive relation is usually employed by assuming isotropic shear viscosity. We adopt this conventional approach, and the second invariants of strain rate and stress ($\dot{\epsilon}_{II}$ and σ_{II}) are assumed in equations (1)–(4). Under this assumption results from simple shear deformation and triaxial compression tests can be analyzed together.

[9] Because diffusion creep and (power law) dislocation creep occur in parallel, the total strain rate of a sample is a simple sum of strain rates due to each mechanism, i.e.,

$$\dot{\epsilon} = \sum_i \dot{\epsilon}_i = \dot{\epsilon}_{\text{diff}} + \dot{\epsilon}_{\text{dis}}, \quad (5)$$

where the subscript i denotes a different deformation mechanism (1 for diffusion creep and 2 for dislocation creep). Roughly speaking, diffusion creep is important at low-stress conditions whereas dislocation creep becomes significant at high-stress conditions. Deformation experiments are usually done at conditions close to a transition between these two mechanisms. Separating contributions from different mechanisms by simultaneous inversion (so-called ‘global’ inversion) is thus important [*Hirth and Kohlstedt*, 2003]. To our knowledge, however, simultaneously inverting for all of the relevant parameters has not been attempted yet for olivine rheology.

[10] For each mechanism, the flow law will depend on the water content. The nature of transition between the “wet” flow law and the “dry” flow law is not very clear since it depends on the details of the microscopic mechanism of deformation. However, in all cases so far studied, strain rate changes with water content (water fugacity) in such a way that the strain rate versus water content curve shows a positive concave shape, and therefore we may choose

$$\dot{\epsilon}_i = \dot{\epsilon}_{i,\text{dry}} + \dot{\epsilon}_{i,\text{wet}} \quad (6)$$

or

$$\dot{\epsilon}_i = \max(\dot{\epsilon}_{i,\text{dry}}, \dot{\epsilon}_{i,\text{wet}}). \quad (7)$$

As in previous studies, we consider dry and wet deformation experiments separately, and use them to determine the

dry and wet flow laws, independently to each other. This is equivalent to assuming equation (7) and also assuming that wet experiments have high enough water concentrations to exceed the transition. This assumption is reasonable because olivines are usually fully saturated with water in wet deformation experiments. We will also test its validity later by inspecting the internal consistency of the estimated flow law (section 4.3).

2.2. Statistical Model For Experimental Data

[11] Both the dry and wet flow laws can be expressed in the form of equation (5), but this equation does not directly lend itself to an inverse problem because experimental data contain various kinds of errors, the functionality of which must also be specified. We propose to use the following simple statistical model for measured strain rate data:

$$\dot{\epsilon}_{\text{obs}}^j = \left(\sum_i \dot{\epsilon}_i(T^j, p^j, d^j, \sigma^j, C_{OH}^j) \right) \exp(X^j), \quad (8)$$

where $\dot{\epsilon}_{\text{obs}}^j$ is a strain rate reported for j -th experiment and X is a random variable. More complicated statistical models are of course possible, but we judge that the above model has sufficient flexibility with respect to existing data. The role of the random variable X is to absorb all of experimental variabilities not explicitly modeled by equations (1)–(4), i.e., variables other than temperature, pressure, average grain size, stress, and water content. Examples include oxygen fugacity, grain size distribution, anisotropy, unnoticed loss of water during a wet experiment, and the duration of an experiment (which is relevant to whether steady state deformation is achieved or not). Oxygen fugacity, for example, may be kept relatively constant in a series of experiments, but different data sets may be characterized by different levels of oxygen fugacity depending on the experimental setup [e.g., *Hirth and Kohlstedt*, 1995a]. Anisotropy in viscosity, though usually not considered, may still exist and develop during deformation, potentially leading to systematic differences among different experimental runs.

[12] This issue of systematic bias has been recognized in the experimental community. For example, the temperature dependency (i.e., activation energy) is usually estimated based on a single experimental run, in which only temperature is changed in a stepwise manner while other parameters are relatively unmodified [e.g., *Mei and Kohlstedt*, 2000a]. An implicit assumption behind this approach is that, whereas the absolute values of strain rate may depend on unquantified experimental parameters, such parameters would remain relatively constant during one experimental run. Relative variations within a single run are thus considered to be robust. In the statistical framework of equation (8), this is equivalent to assume that the random variable X is constant within an experimental run but can take different values among different runs. If this assumption is employed, the variable X may also be called ‘inter-run bias’. This is a strong assumption, but in order to model a more complicated behavior (e.g., ‘drift’ caused by a gradual loss of water), more detailed information on a run condition is required, which is currently unavailable.

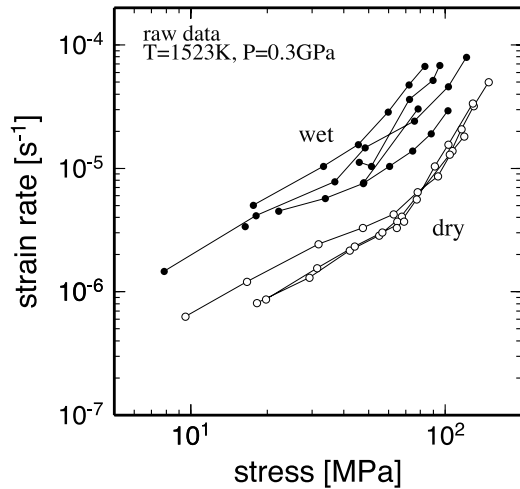


Figure 1. Raw experimental data from *Mei and Kohlstedt* [2000a, 2000b] at $T = 1523$ K and $p = 0.3$ GPa under dry (open circle) and wet (solid circle) conditions. Data from the same run are connected by lines.

[13] A need for the concept of inter-run bias may be apparent in Figure 1. Plotted here are dry and wet experimental runs from *Mei and Kohlstedt* [2000a, 2000b], all conducted at 1523 K and 0.3 GPa (thus no correction for temperature and pressure is required). Dry runs are consistent with each other particularly at high stresses (i.e., in the dislocation creep regime), and the systematic difference seen at lower stresses is due to different grain sizes. A similar consistency is not observed among wet runs. Because all of them are at identical temperature and pressure condition, the water content for wet data is supposed to be the same in principle. As differences in grain size can explain only some minor scatters at low stresses, significant scatters observed at higher stresses (~ 100 MPa) indicate that these experiments are not entirely reproducible due to unspecified experimental variabilities (e.g., loss of water). The importance of inter-run bias will become more obvious when inversion results are shown later.

[14] A misfit between observed and predicted strain rates may be measured by the following cost function:

$$\chi^2(q_k, X_m) = \sum_{m=1}^M \sum_{j_m=1}^{N_m} \frac{\left(\log \hat{\epsilon}_{\text{obs}}^{j_m} - \log \sum_i \hat{\epsilon}_i(s_i^{j_m}) - X_m \right)^2}{\text{rvar}\{\hat{\epsilon}^{j_m}\} + \sum_i \text{rvar}\{i, s_i^{j_m}\}}, \quad (9)$$

where q_k denotes a set of flow-law parameters such as A_i and E_i , and X_m is a set of inter-run biases among M experimental runs, each of which contains N_m deformation data. A set of experimental variables used in the flow law such as T^m and p^m is collectively referred to by s_i^m , and $\text{rvar}\{\hat{\epsilon}^{j_m}\}$ denotes a relative variance originating in the error of strain rate measurements. Finally, $\text{rvar}\{i, s_i^m\}$ denotes a relative variance introduced by the uncertainty of experimental variables in each creep mechanism. When a flow law is estimated in previous studies, a linear regression is usually used. For example, strain rates are plotted as a function of deviatoric stress, and a stress exponent is

estimated by minimizing misfit only in the vertical coordinate (i.e., strain rate). This corresponds to neglecting $\text{rvar}\{i, s_i^m\}$, the consideration of which makes the inverse problem highly nonlinear. There are, however, small but finite errors in all of experimental variables, which must be taken into account when fitting a flow law to experimental data. Each error may be small, but their sum may not be so. When there are only two variables, this is a well-known problem in statistics called least squares with errors in both coordinates [e.g., *Deming*, 1943; *Reed*, 1989; *Macdonald and Thompson*, 1992]. Equation (9) can be derived by generalizing it to many variables.

[15] In equation (9), strain rates are compared in the logarithmic scale, because the uncertainty of strain rate measurements is usually provided in the form of relative error. To be consistent with this, the first term in the denominator is defined as:

$$\text{rvar}\{\hat{\epsilon}^j\} = \frac{\text{var}\{\hat{\epsilon}^j\}}{(\hat{\epsilon}_{\text{obs}}^j)^2}, \quad (10)$$

where $\text{var}\{\hat{\epsilon}^j\}$ is the variance (or squared error) of j -th strain rate data (see Appendix A). Thus if its relative measurement error is 5%, $\text{rvar}\{\hat{\epsilon}^j\}$ is $(0.05)^2 = 0.0025$. The second term is more complex, and its derivation is given in Appendix A. For diffusion creep under dry conditions ($i = 1$), for example, we have

$$\text{rvar}\{1, s_1^j\} = \left(\frac{\hat{\epsilon}_1^j}{\sum_i \hat{\epsilon}_i^j} \right)^2 \left(p_1^2 \frac{\text{var}\{d^j\}}{(d^j)^2} + \frac{\text{var}\{\sigma^j\}}{(\sigma^j)^2} + \left(\frac{V_1}{RT^j} \right)^2 \text{var}\{p^j\} + \left(\frac{E_1 + p^j V_1}{R(T^j)^2} \right)^2 \text{var}\{T^j\} \right), \quad (11)$$

where the index i runs from 1 (dry diffusion creep) to 2 (dry dislocation creep). Note that this variance depends not only on experimental variables and their uncertainty but also on flow-law parameters.

[16] The cost function is a function of not only flow-law parameters q_k but also inter-run biases X_m , both of which are to be estimated by minimizing this cost function. We will treat this nonlinear inverse problem by a Bayesian approach.

2.3. Bayesian Inference

[17] We call q_k and X_m collectively as a model \mathbf{m} , and a space spanned by all possible models is denoted by \mathcal{M} . Our task is more than just minimizing $\chi^2(\mathbf{m})$ over \mathcal{M} ; we need to delineate the model subspace that contains all of equally ‘successful’ models in terms of explaining given experimental data. Even before looking at data, we have some (albeit vague) idea on the likely range of successful models. For example, activation energies E_i should be positive and are probably on the order of a few hundreds kJ mol^{-1} . The model space we need to explore is bounded by such a priori constraints and not infinite. By incorporating experimental

constraints (i.e., calculating $\chi^2(\mathbf{m})$), we can further restrict the model space.

[18] Bayesian inference formalizes the above procedure as follows [e.g., Tarantola, 1987]. Let us define

$$\rho(\mathbf{m}) = k p(\mathbf{m}) L(\mathbf{m}), \quad (12)$$

where $\rho(\mathbf{m})$ is the a posteriori probability density, k is a normalization constant, $p(\mathbf{m})$ is the a priori probability density, and $L(\mathbf{m})$ is the likelihood function that measures the success of a particular model by comparing its predictions with observations. The a priori probability density $p(\mathbf{m})$ can take a simple form, e.g., $p(\mathbf{m}) = c$ (c is a normalization constant) if all of model parameters are within prescribed bounds and $p(\mathbf{m}) = 0$ otherwise. It is common to calculate the likelihood function based on the cost function as

$$L(\mathbf{m}) = \exp\left(-\frac{1}{2}\chi^2(\mathbf{m})\right), \quad (13)$$

and we also adopt this definition. The normalization constant k is determined so that

$$\int_{\mathcal{M}} \rho(\mathbf{m}) d\mathbf{m} = 1. \quad (14)$$

With the a posteriori probability density, the model mean can be calculated as:

$$\text{mean}\{\mathbf{m}\} = \int_{\mathcal{M}} \mathbf{m} \rho(\mathbf{m}) d\mathbf{m}, \quad (15)$$

and the model variance is given by

$$\text{var}\{\mathbf{m}\} = \int_{\mathcal{M}} (\mathbf{m} - \text{mean}\{\mathbf{m}\})^2 \rho(\mathbf{m}) d\mathbf{m}. \quad (16)$$

[19] Estimating the flow-law parameters and their uncertainty thus reduces to evaluating the integrals of equations (15) and (16). This integration is, however, difficult because of the high dimensionality of our problem. The composite flow law under dry conditions, for example, has eight parameters (equations (1) and (3)), and because there are 14 relevant experimental runs in published data (so 13 biases to estimate), the total number of model parameters is 21. Even if we discretize each dimension very coarsely using only 10 points, we have to evaluate the integrand for 10^{21} different models at least. Such brute-force numerical integration is obviously intractable and also extremely inefficient; the likelihood function $L(\mathbf{m})$ and thus $\rho(\mathbf{m})$ is virtually zero for most models because of their large $\chi^2(\mathbf{m})$. We are thus forced to sample the model space by some kind of Monte Carlo scheme, but sampling should be much more efficient than purely random. Markov chain Monte Carlo methods would be optimal for our purpose.

2.4. Markov Chain Monte Carlo With Gibbs Sampler

[20] Markov chain Monte Carlo (MCMC) methods are a class of algorithms for sampling from a probability distribution based on Markov chains [e.g., Liu, 2001; Robert and Cassela, 2004]. Being very powerful for numerically calculating multidimensional integrals, these algorithms have a

long history in computational physics [e.g., Metropolis et al., 1953; Frenkel and Smit, 2002] and have become popular in Bayesian statistics in recent years. MCMC applications can also be found in geophysical inverse problems [e.g., Mosegaard and Tarantola, 1995; Sambridge and Mosegaard, 2002]. There are a number of excellent articles and books on MCMC methods [e.g., Geyer, 1992; Smith and Roberts, 1993; Gilks et al., 1996; Gamerman, 1997; Liu, 2001; Robert and Cassela, 2004], and readers are referred to those references for formal and rigorous explanations. Here we restrict ourselves to discussing two major sampling schemes, the Metropolis algorithm and the Gibbs sampling, in the context of our inverse problem.

[21] In the Metropolis algorithm, we choose arbitrarily an initial model, \mathbf{m}_0 , and calculate corresponding $\rho(\mathbf{m}_0)$. We then randomly perturb this initial guess to get a trial model, \mathbf{m}' , and calculate $\rho(\mathbf{m}')$. If $\rho(\mathbf{m}') > \rho(\mathbf{m}_0)$, \mathbf{m}' is certainly a better model than \mathbf{m}_0 , so we accept this perturbed model as the next model, i.e., $\mathbf{m}_1 = \mathbf{m}'$. If $\rho(\mathbf{m}') \leq \rho(\mathbf{m}_0)$, on the other hand, we draw one random number, r , from the interval $[0,1]$ and

$$\mathbf{m}_1 = \begin{cases} \mathbf{m}' & \text{if } r < \rho(\mathbf{m}')/\rho(\mathbf{m}_0), \\ \mathbf{m}_0 & \text{otherwise.} \end{cases} \quad (17)$$

Even if a trial move does not result in a better model, therefore, there is a finite possibility that it is accepted as the next move. The theory of Markov chains guarantees that, roughly speaking, the repeated application of this random move eventually explores all ‘important’ models (i.e., ones with reasonably high $\rho(\mathbf{m})$). When such situation is achieved, the random walk is said to be ‘converged’.

[22] We do not know, however, how many iterations are necessary to reach convergence a priori, and the number of required iterations often depends heavily on how random walk is simulated. In general, the size of random perturbation to create a trial move must be small enough so that successive moves do not result in drastic model changes, which usually result in rejecting most trial moves, but also large enough to avoid being trapped near a local minimum for a long time. That is, the perturbation size should be carefully chosen so that a corresponding Markov chain has rapid ‘mixing’. It requires trial and error to tune the Metropolis step, and this tuning is often data-dependent; the best tuning for a particular data set does not necessarily work well for different data sets. Also, different model parameters need different optimal steps. This trial-and-error approach becomes quite cumbersome when the number of model parameters is large.

[23] On other hand, the Gibbs sampling, which is based on the conditional distributions of the target distribution ($\rho(\mathbf{m})$ in our case), does not require any tuning. Moreover, a model perturbation is always global in this scheme. Though additional sampling is required to estimate the conditional distributions, we find the Gibbs sampling more appealing, and our MCMC implementation is based on the so-called random-scan Gibbs sampler [e.g., Liu, 2001].

[24] We choose to express a priori model constraints as upper and lower limits on model parameters $\mathbf{m} = \{m_k | k = 1, 2, \dots, K\}$, i.e.,

$$m_k^L \leq m_k \leq m_k^U. \quad (18)$$

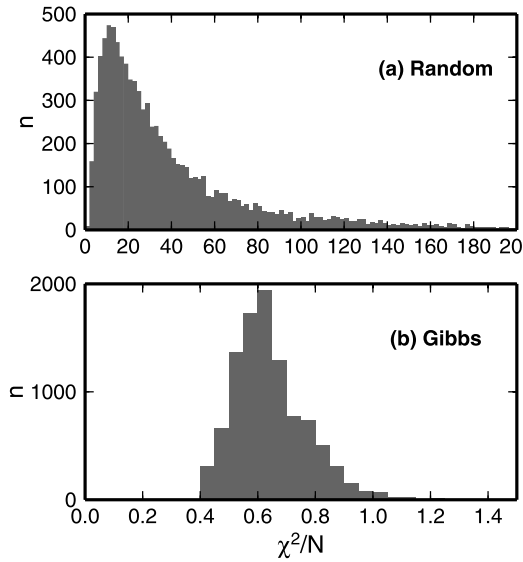


Figure 2. The distribution of χ^2/N for two different sampling schemes: (a) purely random sampling and (b) Gibbs sampling. Shown here is for the MCMC simulation with the dry deformation data from MK00 (see section 4.1 for a full description).

By keeping a Markov chain within these bounds, model sampling is automatically restricted where $p(\mathbf{m}) = c (\neq 0)$. This sampling with the a priori probability can considerably enhance the efficiency of MCMC simulation [e.g., *Mosegaard and Tarantola, 1995*], but our problem has one unique difficulty to overcome; there are no useful a priori bounds on the scaling constants A_i in equations (1)–(4). Because the activation energy and volume are within the exponential function, even small changes in them could enormously change the magnitude of these scaling constants. Thus even though we can derive bounds on the scaling constants based on the bounds of activation energy and volume, such bounds range over many orders of magnitudes and are simply too wide to be useful. Having the scaling constants in a proper range is, however, essential for data fitting. Otherwise, quite a large number of samplings would be wasted because of unacceptably large χ^2 , and a MCMC simulation would be very inefficient. For this reason, we treat the scaling constants differently from the rest of model parameters. A short summary on this special treatment is the following (see Appendix B for details). When model parameters other than the scaling constants are given, we first calculate the ‘best fit’ constants by standard linear regression because the flow law (equation (5)) is linear in A_i . By standard linear regression, however, model-dependent variances (e.g., $\sum_i \text{rvar}\{i, s_i^m\}$ in equation (9)) are ignored, so the resulting constants are not best fit in terms of the cost function defined with all of experimental uncertainties. We then randomly perturb these ‘best fit’ constants within prescribed bounds. Thus we do have a priori constraints on all of model parameters, but our bounds on the scaling constants are indirect. When m_k corresponds to a scaling constant, it should be interpreted as a perturbation to the linear regression result, and equation (18) as bounds on such perturbation. Note that linear regression is used here

only to accelerate MCMC simulations; it does not mean that we are linearizing our inverse problem or introducing additional assumptions.

[25] Important steps in our MCMC simulation are summarized below. For a pseudo-random number generator, we use Numerical Recipes’ `ran2` function [*Press et al., 1992*].

[26] 1. **Initialization.** Draw K random numbers, r_k , from the interval $[0,1]$ to set the initial model as

$$m_{0,k} = m_k^L + r_k(m_k^U - m_k^L),$$

for $k = 1, 2, \dots, K$.

[27] 2. **Random scan.** Pick one model parameter randomly from $\{m_k | k = 1, 2, \dots, K\}$ and call it m_r . The random-scan Gibbs sampling requires that we know the conditional likelihood:

$$L(\{m_{0,1}, \dots, m_{0,r-1}, m_r, m_{0,r+1}, \dots, m_{0,K}\}).$$

All parameters other than m_r are fixed as in the current model \mathbf{m}_0 , and the conditional likelihood is a function of m_r only. From the interval $[m_r^L, m_r^U]$, we draw P random numbers and calculate corresponding likelihood values. When P is sufficiently large, we can approximate the conditional likelihood function by the rejection sampling [*von Neumann, 1951*]. Save the highest likelihood as L_{\max} .

[28] 3. **Gibbs sampling.** Pick one random number from the interval $[m_r^L, m_r^U]$ and call it m'_r . Construct a trial model:

$$\mathbf{m}' = \{m_{0,1}, \dots, m_{0,r-1}, m'_r, m_{0,r+1}, \dots, m_{0,K}\}$$

and calculate $L(\mathbf{m}')$. Draw one more random number, s , from the interval $[0,1]$. If $s < L(\mathbf{m}')/L_{\max}$, go to the next step. Otherwise, start over this step.

[29] 4. **Model update.** Save the old model \mathbf{m}_0 and redefine it with \mathbf{m}' . Until the maximum number of iteration is reached, go back to step 2.

[30] The efficiency of Gibbs sampling may be seen in Figure 2, which compares the distribution of normalized χ^2 (i.e., χ^2/N where N is the total number of data) for the cases of purely random sampling and Gibbs sampling. If random sampling is not guided in any sense, the bulk of sampling is spent in the unimportant parts of the model space. The Gibbs sampling, on the other hand, explores important models very effectively. A similar success can also be achieved by other guided sampling schemes such as the Metropolis algorithm, but we emphasize that the Gibbs sampling does not require any tuning and is also global. We use $P = 100$ to estimate the conditional distributions that arise in the Gibbs sampling, and this hidden cost is well compensated by this ease of use and by the success in quickly collecting only good models from the entire model space.

[31] If we denote our MCMC solutions and their misfits by \mathbf{m}_q and χ_q^2 , respectively, the model mean under the normalization constraint (equations (14) and (15)) can be approximated as

$$\text{mean}\{\mathbf{m}\} \approx \frac{\sum_{q=1}^Q \mathbf{m}_q \exp(-\chi_q^2/2)}{\sum_{q=1}^Q \exp(-\chi_q^2/2)}, \quad (19)$$

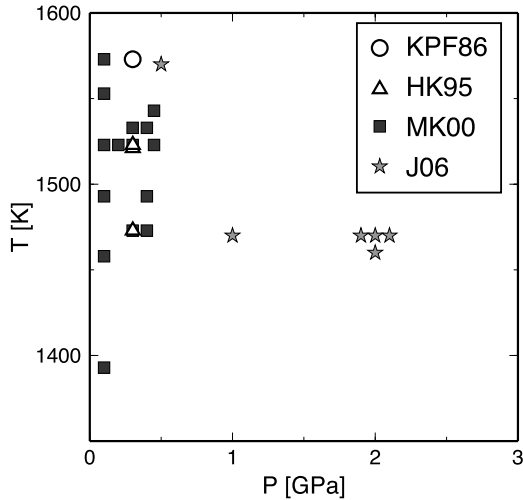


Figure 3. Pressure and temperature conditions for the four experimental studies compiled for this study: KPF86 [Karato *et al.*, 1986] (circle), HK95 [Hirth and Kohlstedt, 1995a] (triangle), MK00 [Mei and Kohlstedt, 2000a, 2000b] (square), and J06 [Jung *et al.*, 2006] (star).

where Q is the total number of MCMC solutions. Other statistical estimators can be approximated in a similar manner. The scaling constants A_i need a special care; they are tightly coupled with other parameters, especially activation energies, and vary over many order of magnitudes. Their direct statistics is thus not very useful, even if done in the logarithmic scale. We try to reduce its variation by removing contribution from concurrent changes in other parameters as:

$$B_i = \log_{10} \left(A_i \exp \left(-\frac{E_i + p_0 V_i}{RT_0} \right) \right), \quad (20)$$

where T_0 is 1523 K and p_0 is 0.3 GPa. This conversion is important to have a compact distribution for the scaling constants.

[32] Note that the inter-run biases, X_M , are so-called ‘nuisance’ parameters in statistics. They are not what we really want to know, i.e., not a part of the flow law we seek to establish, but they still need to be determined to get the flow law right. The nuisance parameters can be integrated out by marginalization as:

$$\rho(q_k) = \int_{\mathcal{M}_X} \rho(q_k, X_M) dX_M, \quad (21)$$

where \mathcal{M}_X denotes the model space for X_M . In our approximating strategy with MCMC solutions (e.g., equation (19)), this corresponds to simply using all solutions irrespective of the value of X_M .

3. Data

[33] We compiled all of published subsolidus deformation experiments on synthetic olivine aggregates with composi-

tions similar to Earth’s mantle ($\sim\text{Fo}_{90}$) [e.g., Hart and Zindler, 1986; McDonough and Sun, 1995]. Our compilation consists of four different data sets: Karato *et al.* [1986] (hereinafter referred to as KPF86), Hirth and Kohlstedt [1995a] (HK95), Mei and Kohlstedt [2000a, 2000b] (MK00), and Jung *et al.* [2006] (J06). Note that the experiments briefly reported by Karato and Jung [2003] are fully described in J06. We avoid including experiments with natural dunites [e.g., Chopra and Paterson, 1984] because controlled experiments are usually more difficult with such samples. Experiments with pure forsterite [McDonnell *et al.*, 1999] are also excluded because point defect chemistry and thus kinetic properties appear to be very different between forsterite (Fo_{100}) and mantle olivine (Fo_{90}) [Mei and Kohlstedt, 2000a]. Two high-pressure (2 GPa) experiments under a dry condition are reported by Jung and Karato [2001] but not included here because of extreme heterogeneity in grain size distribution. There are more recent data on dry olivine rheology using X-ray diffraction techniques up to 11 GPa [e.g., Li *et al.*, 2004; Y. Nishihara *et al.*, Plastic deformation of wadsleyite and olivine at high-pressures and high-temperatures using a rotational Drickamer apparatus (RDA), submitted to *J. Geophys. Res.*, 2007], but they are also excluded because the nature of uncertainties in these high-pressure studies is not yet well understood. We will discuss later the significance of these excluded high-pressure data on the basis of supplementary inversions.

[34] The four data sets differ in various aspects of experimental design and conditions. For example, KPF86 and J06 are constant strain rate experiments whereas HK95 and MK00 are constant load experiments. The identification of ‘steady state’ is not straightforward in constant stress experiments [e.g., Karato, 2007, Chap. 6], and we assume steady state deformation for HK95 and MK00. The experimental geometry is triaxial compression for KPF86, HK95, and MK00, and simple shear for J06. In comparing results from experimental data for different deformation geometry, we make an assumption of isotropic plasticity and use the Levy-von Mises formula [e.g., Karato, 2007, Chap. 3]. KPF86 was conducted at single temperature and pressure (1573 K and 0.3 GPa). Later studies were conducted over a range of temperature and pressure (Figure 3), so they are useful to constrain activation energy and volume. However, we should expect large uncertainty in those parameters because ranges so far explored are still narrow. Oxygen fugacity is controlled by the Fe-FeO buffer in KPF86 and the Ni-NiO buffer in others. The activity of silica is fixed by the presence of a small amount of enstatite, except for KPF86. These differences in the chemical environment may cause systematic bias in strain rates [e.g., Hirth and Kohlstedt, 1995a]. In addition, the presence of melt is not very well constrained. We chose the results from ‘melt-free’ samples, but a small amount of melt ($<0.1\%$) is hard to detect although it may have an important effect on deformation [Takei and Holtzman, 2006].

[35] Deformation experiments are usually run at either ‘dry’ or ‘wet’ condition. The dry condition is also referred to as ‘nominally anhydrous’, because a sample may still contain a trace amount of water below the detection limit of FTIR (Fourier transformation infrared spectroscopy). Under the wet condition, samples are fully saturated with water, if free water is present during an experiment. If this condition

Table 1. Summary of Experimental Errors

	δT	δP	$\delta \sigma$	$\delta \dot{\epsilon}$	δd	δC_{OH}
<i>Karato et al.</i> [1986]	10 K	5 MPa	2 MPa	1%	10%	20%
<i>Hirth and Kohlstedt</i> [1995a]	2 K	4 MPa	2 MPa	5%	10%	- ^a
<i>Mei and Kohlstedt</i> [2000a, 2000b]	2 K	4 MPa	2 MPa	5%	10–30%	20%
<i>Jung et al.</i> [2006]	10 K	10%	15%	9–23%	10%	20%

^aAll data of HK95 are from ‘dry’ experiments.

is met, then one can calculate the water content in the sample from the experimental results of water solubility [e.g., *Kohlstedt et al.*, 1996; *Zhao et al.*, 2004]. As the formula of *Zhao et al.* [2004] is based on the new FTIR calibration by *Bell et al.* [2003], we also adopt this calibration and multiply a factor of 3.5 to the water content data of KPF86 and J06, which are based on the traditional calibration by *Paterson* [1982]. The choice of calibration is merely a matter of convention here; our estimated flow law could easily be modified for a different calibration by trivial changes in the scaling constants A_i . Note that the assumption of saturation with water was confirmed in some studies (e.g., KPF86 and J06) but not in others such as MK00. This could cause systematic errors as we will discuss later.

[36] KPF86, HK95, and MK00 used a gas-medium apparatus with an internal load cell (e.g., the Paterson apparatus). We note that the resolution of mechanical data is much higher for those gas-medium apparatus data than for results using any other techniques. However, there are major limitations with the data from this type of apparatus. Most important is the limitation in the maximum pressure (~ 0.5 GPa). Because the water effect is highly sensitive to the total pressure, which changes water fugacity, and because the nature of water changes from nearly ideal gas below ~ 0.5 GPa to highly non-ideal gas above ~ 0.5 GPa, it is critical to use data spanning a pressure range over ~ 0.5 GPa [*Karato*, 2006]. In addition, the determination of the pressure effect (at a constant water fugacity or water content) also requires a large span of pressure because the pressure effect is exponential. However, quantitative experimental studies on high-temperature rheology are challenging and currently available data at pressures beyond 0.5 GPa is limited. At present, the only data on water effects beyond 0.5 GPa is from J06 (up to 2 GPa), which were obtained with a Griggs apparatus. Though the uncertainty in these data is worse than obtained using a gas-medium apparatus, data to constrain both water and pressure effects can be obtained only from these experiments at present. We note that in addition to the poorer resolution in stress and strain rate measurements by this high-pressure study, another complication is a possible bias caused by plastic anisotropy. Currently, little is known about plastic anisotropy in olivine aggregates. The few data obtained by *Zhang et al.* [2000] suggest a weak anisotropy that depends on the degree of dynamic recrystallization. In this study, we make the admittedly rough approximation of plastic isotropy, the validity of which needs to be evaluated in future. The main purpose of this study is to explore the importance of a rigorous statistical analysis using a broad range of experimental data, and we emphasize that our conclusions depend critically on the chosen data sets as well as the assumptions employed.

[37] Our compilation includes 14 experimental runs with 81 data under dry conditions (six runs from KPF86, three from HK95, and five from MK00), and 26 runs with 130 data under wet conditions (10 from KPF86, 15 from MK00, and one from J06). We use only nominally melt-free data from HK95 (PI-35, PI-146, and PI-81). More melt-free data are reported in their companion paper [*Hirth and Kohlstedt*, 1995b], but their grain sizes have not been measured (*G. Hirth*, pers. comm., 2006), so they cannot be used for our global inversion. MK00 is the largest data set, providing 127 deformation data (35 dry and 92 wet data). MK00 reports only the initial and final grain sizes for multistep experimental runs, and we use the grain growth equation of *Karato* [1989] to interpolate between them. Some of their experiments do not report even these bounding grain sizes, but initial and final (average) grain sizes were usually 15 ± 1 microns and 18 ± 1 microns, respectively (*S. Mei*, pers. comm., 2006), so we supplement grain size data accordingly with additional uncertainty. Note that we only consider uncertainty in *average* grain size, which is usually smaller than the standard deviation of grain size distribution. J06 reports 17 data, but some of them suffer from major experimental difficulties. After grain size information was supplemented (*H. Jung*, pers. comm., 2006), only seven of them (JK11, JK18, JK24, JK26, JK40, JK41, JK43) were found to be appropriate for our purpose.

[38] Note that an experimental run should contain more than one data point; otherwise, a misfit between data and flow-law prediction could completely be absorbed by $\exp(X_m)$, and such a run does not contribute to constrain the flow law in the present framework. In other words, a single deformation datum alone cannot prove its reproducibility. For this reason, runs 4604, 4688, 4885, and 4920 in KPF86 and PI-17 in HK95 are excluded. None of experimental runs in J06 contains more than one deformation datum, so J06 data are collectively treated as one experimental run in our compilation. In this case, we are assuming that there is no inter-run bias among J06 data, but that there can be some systematic differences with respect to other deformation data.

[39] The uncertainties of experimental variables are summarized in Table 1. Most of them are reported in the original publications, and the rest is supplemented by personal communication. The uncertainty of stress is notably high for J06 because stress is estimated through an empirical correlation with dislocation density. We are conservative about the accuracy of grain size and assign 10% uncertainty. For MK00, we add another 10% uncertainty when initial or final grain size is missing and has to be roughly estimated as mentioned above. The accuracy of water content is limited by that of FTIR, and we set the uncertainty to 20% [*Koga et al.*, 2003]. As discussed above, the actual uncertainties of water content could be

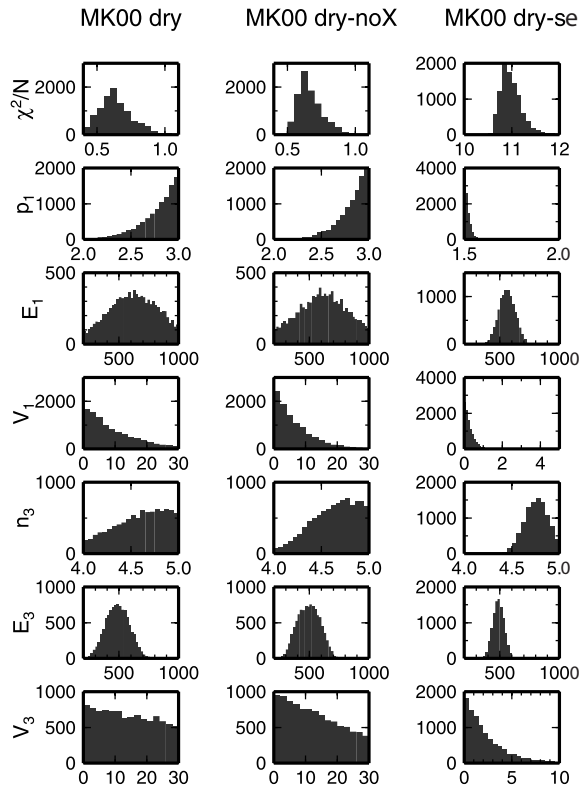


Figure 4. Histograms of 10^4 MCMC solutions with the dry MK00 data: (left) the standard simulation, (middle) the simulation with no inter-run biases, and (right) the simulation with neglecting $\text{rvar}\{i, s_i^m\}$.

much larger, and the inter-run bias $\exp(X_m)$ tries to absorb such ‘hard-to-quantify’ uncertainties.

4. Results

[40] In this section, we present a series of MCMC simulations on different data sets with a variety of simulation constraints. To facilitate the understanding of this new approach, we start with showing our inversion results for a small subset of the compiled data and progressively approach the most comprehensive inversion. The robustness of our final results may be understood by comparing different inversion results.

[41] The dry and wet versions of the olivine flow law were estimated separately. For any type of inversion, we ran ten parallel MCMC simulations with different starting models, and each run consists of 10^6 Gibbs sampling. Because starting models were constructed randomly, they usually had very large data misfits, but the misfit quickly decreased as the iteration proceeds. To ignore bad models in this early stage, we discarded the first 10^4 samples. Moreover, because the random-scan algorithm changes only one parameter per step, neighboring steps were closely correlated so we sampled every 10^3 models to gather more uncorrelated models. For each inversion, therefore, we have $\sim 10^4$ MCMC ensembles.

[42] The a priori bounds on model parameters are as follows: $1.5 \leq p_i \leq 3$, $2 \leq n_i \leq 5$, $0.5 \leq r_i \leq 2$, $100 \leq E_i \leq 1000$ (in kJ mol^{-1}), $0 \leq V_i \leq 30$ (in $\text{cm}^3 \text{mol}^{-1}$), $10^{\pm 1}$

bounds on perturbations to ‘best fit’ A_i , and $10^{\pm 0.5}$ bounds on inter-run biases $\exp(X_m)$. For most of these parameters, there is no real theoretical bound, and the above ranges were chosen to encompass so far proposed values [e.g., *Bai et al.*, 1991; *Karato and Wu*, 1993; *Mei and Kohlstedt*, 2000a; *Hirth and Kohlstedt*, 2003]. As shown later, results with wider bounds suggest that the a priori bounds are essential to obtain a stable estimate for some model parameters. In this case, the a priori bounds may be regarded as one form of regularization, which can guarantee a ‘sensible’ flow law even from noisy data.

[43] Whereas the statistical distribution of a large number of MCMC ensembles fully describes our current knowledge of olivine deformation, it would be more convenient to have a more compact representation. After demonstrating the convergence of our MCMC simulations, we seek to establish such a representation by combining the principal component analysis and linear regression.

4.1. Rheology of Dry Olivine Aggregates

[44] The five experimental runs from MK00 (PI-181, PI-220, PI-360, PI-394, PI-567) were conducted at varying temperature and pressure conditions, so in principle one can invert for all of relevant flow-law parameters. Before using all of experimental runs from different research groups, it would be instructive to see how our inversion works for the MK00 data alone and how well they can constrain those parameters.

[45] Among those five runs, PI-181, PI-394, and PI-567 were all conducted at 1523 K and 0.3 GPa. PI-220 was also at 1523 K, but the pressure was varied from 0.1 to 0.3 GPa, under relatively low stress conditions. PI-360 was at 0.3 GPa, and the temperature was varied from 1473 K to 1573 K under high stress conditions. Therefore we expect that this data set could potentially constrain the pressure dependency for dry diffusion creep (i.e., V_1) and the temperature dependency for dry dislocation creep (i.e., E_3) but provides only indirect and weak constraints on V_3 and E_1 (note that diffusion creep is always activated, even at high stresses, so the data have non-zero sensitivity to E_1).

[46] In addition to the standard MCMC simulation, we conducted two more simulations, one fixing inter-run biases to zero (“-noX”) and the other ignoring all parameter uncertainties other than for strain rates (“-se” for ‘simplified error’). Note that inter-run biases were still modeled in the latter. The results of these three inversions are compared in Figure 4, in terms of the distribution of the corresponding MCMC solutions.

[47] The normalized χ^2 for the standard simulation is clustered around ~ 0.6 , indicating that the given data are fitted by an estimated flow law within uncertainty on average. The grain-size exponent p_1 is estimated to be ~ 3 , and the activation energy for dislocation creep is $\sim 500 \text{ kJ mol}^{-1}$, both of which are in good agreement to the original estimate by *Mei and Kohlstedt* [2000a, 2000b]. The activation volume for diffusion creep (V_1) appears to favor low values ($< 10 \text{ cm}^3 \text{mol}^{-1}$). One notable difference from previous studies [*Mei and Kohlstedt*, 2000b; *Hirth and Kohlstedt*, 2003] is the stress exponent n_3 , for which a relatively high value (~ 5) is preferred, whereas the canonical value has long been considered to be ~ 3.5 . As expected, other parameters (E_1 and V_3) are much more

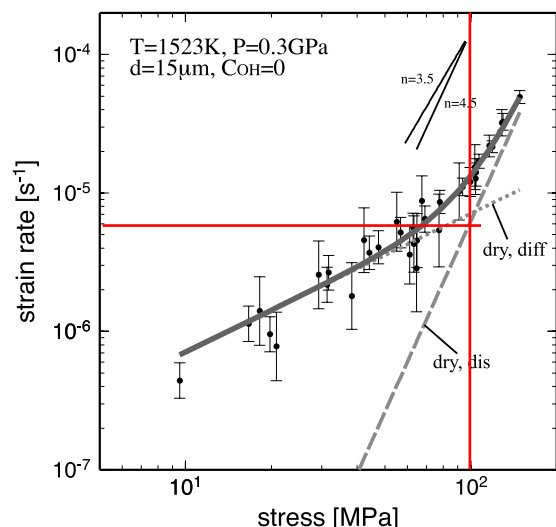


Figure 5. Stress vs. strain rate relationship for the dry MK00 data normalized at the reference dry condition, shown with best fit flow laws. The error bar of strain rate includes all other experimental uncertainties. Bias correction is also applied.

loosely constrained. Inter-run biases are estimated to be small, in the range of $10^{-0.15}$ to $10^{0.06}$ (with the run PI-181 as a reference). From this, one would expect that imposing zero bias should not result in a very different flow law, and this is indeed the case (Figure 4, middle panel). On the other hand, neglecting the uncertainties of temperature, pressure, grain size, and stress resulted in a substantially different estimate (Figure 4, right panel). First of all, the normalized χ^2 is far greater than unity, suggesting that the assumed statistical model misses some important sources for data misfit. Second, the distribution of MCMC solutions is much more sharply defined, giving a false impression that the flow-law parameters are tightly constrained. Accounting for all of experimental uncertainties is important to properly define the extent of the permissible parameter space.

[48] All of these simulations consistently show that the best fit stress exponent n_3 is noticeably higher than 3.5, and the mean value from the standard simulation is ~ 4.58 . In Figure 5, all data are normalized to our reference dry conditions ($T = 1523$ K, $p = 0.3$ GPa, and $d = 15$ μm) and are compared with the best fit flow law based on the standard simulation. In this figure, all of experimental uncertainties are summed into the error bars of strain rate. We use this simple visualization throughout this paper. Note that this is for plotting purposes only, and we are not redefining the uncertainty of strain rate. Figure 5 indicates that diffusion creep has a nontrivial contribution even at the highest stress produced, so the determination of the stress exponent relies heavily on how accurately diffusion creep is estimated, or more precisely, how properly a global inversion is set up. Whether the exponent is 3.5 or 4.5 may be a subtle issue in terms of fitting data (see Figure 5), but this difference corresponds to two orders of magnitude difference in effective viscosity when extrapolating from 100 MPa to 1 MPa. The estimated stress exponent suggests that dislocation creep under dry conditions may be controlled

by slip on the (010)[001] system [Bai *et al.*, 1991, Table 1]. Another possibility is that high stress data may also be influenced by the Peierls mechanism, which could make the stress exponent apparently high. To test this idea, we also conducted another set of MCMC simulation by restricting data to $\sigma_{II} < 100$ MPa (or $\sigma_1 - \sigma_3 < 173$ MPa), but our inference on n_3 became only more blurred, with no particular preference toward a lower value.

[49] We then proceeded to include the rest of the dry deformation data. Figure 6 compares the results with three different data sets (MK00 only, MK00 + HK95, and MK00 + HK95 + KPF86 (“all dry”). Also shown is the result for all data but with wider a priori bounds (“-wb”) on some parameters ($\max(p) = 5$, $\max(n) = 6$, and $\max(V) = 60$). The normalized χ^2 increased to ~ 2 when the HK95 data were included. Ideally, we would like to have $\chi^2/N < \sim 1$, so this slightly large misfit may indicate that merging different data sets requires more than simple bias correction. It is probably too simplistic to expect that a single number $\exp(X_m)$ to absorb all factors related to inter-run differences.

[50] Figure 6 shows that our inference gradually sharpens as we add more experimental runs, most notably for p_1 , E_1 , and n_3 . The simulation with the wider bounds, however, reveals that the tight distribution of the grain-size exponent at ~ 3 is simply because of the a priori upper bound. When the upper bound was extended to 5, the distribution shifted to the new bound. This implies that $p_1 \sim 3$ is not demanded by the data; it is merely the best choice from the given range

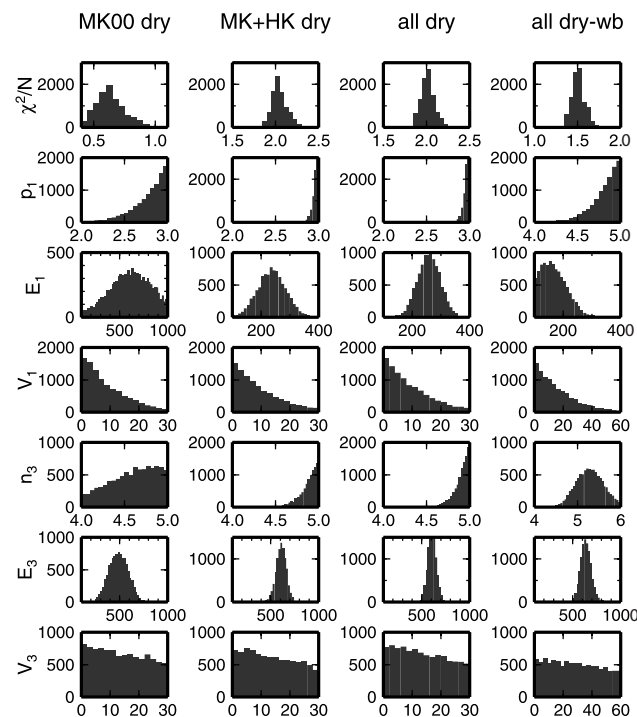


Figure 6. Histograms of 10^4 MCMC solutions from four different simulations with dry experimental runs. “MK00 dry” is the same as shown in the left panel of Figure 4. “MK + HK dry” is the simulation with the MK00 and HK95 data. “all dry” and “all dry-wb” are the simulations with all of dry experimental runs with the standard and extended a priori bounds, respectively.

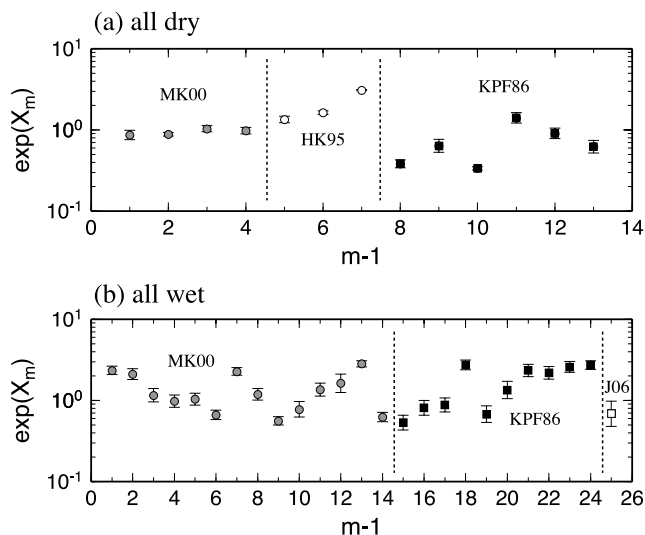


Figure 7. Mean values and one standard deviations for estimated inter-run biases for (a) “all dry” and (b) “all wet” simulations, plotted as a function of experimental run id, m .

(from 1.5 to 3). In other words, the given data do not have enough resolution to keep the grain-size exponent within a theoretically plausible range. There seems to be some trade-off between p_1 and E_1 , and the proper a priori bounds on p_1 are important for a stable inversion. On the other hand, $n_3 \sim 5$ appears to be more robust. The activation volumes remain poorly constrained even with all data.

[51] Inter-run biases (with respect to MK00’s PI-181) estimated by the standard simulation with all dry data are shown in Figure 7a. The strain rates from HK95 are generally higher than those from MK00, whereas KPF86 data tend to have lower strain rates. Bias correction was not important for the inversion with the MK00 data alone, but it is essential for this larger data set.

[52] Because the activation volumes V_1 and V_3 are so poorly constrained, we also conducted two exploratory MCMC simulations including the high-pressure deformation data of *Jung and Karato* [2001]. The runs JK19 and JK21 are collectively referred to as the JK01 data. As noted in section 3, this data set is characterized by highly heterogeneous grain-size distributions. In the dislocation creep regime, grain size was controlled by dynamic recrystallization, but under a dry condition, the kinetics of this recrystallization was so slow that it was difficult to achieve a steady state, homogeneous grain-size distribution during a deformation experiment. JK01 used a single crystal as a starting material, and the reported grain size of $\sim 3 \mu\text{m}$ refers to the average grain size of partially recrystallized regions. Thus an ‘effective’ grain size for the deformed sample as a whole could be higher. We first ran a simulation with the reported grain sizes (“all + J dry”), and then ran another simulation with the grain sizes increased by a factor of ten (“all + Jx dry”). The results are compared with the standard “all dry” simulation in Figure 8.

[53] Adding the high-pressure data drastically modified the estimate of activation volumes. Both activation volumes (V_1 and V_3) are clustered around the upper bound ($30 \text{ cm}^3 \text{ mol}^{-1}$) for the “all + J” simulation. The high activation

volume for diffusion creep is most likely due to taking the reported grain size at face value, because increasing the grain size by a factor 10 (“all + Jx”) brings our inference on V_1 back to a much less constrained distribution, virtually identical to what is obtained without the high-pressure data. This amplification of grain size is an arbitrary manipulation and should be regarded as a simplistic sensitivity test, but it successfully placed the JK01 data into the dislocation creep regime without deteriorating our estimate on diffusion creep. The high activation volume for dry dislocation creep ($V_3 \sim 25\text{--}30 \text{ cm}^3 \text{ mol}^{-1}$) appears to be robust. This is in direct conflict with what has been suggested by more recent experimental studies at higher pressures [e.g., *Li et al.*, 2004].

4.2. Rheology of Wet Olivine Aggregates

[54] To establish the olivine flow law under wet conditions, we proceeded in a similar manner to the previous section. We first conducted three types of MCMC simula-

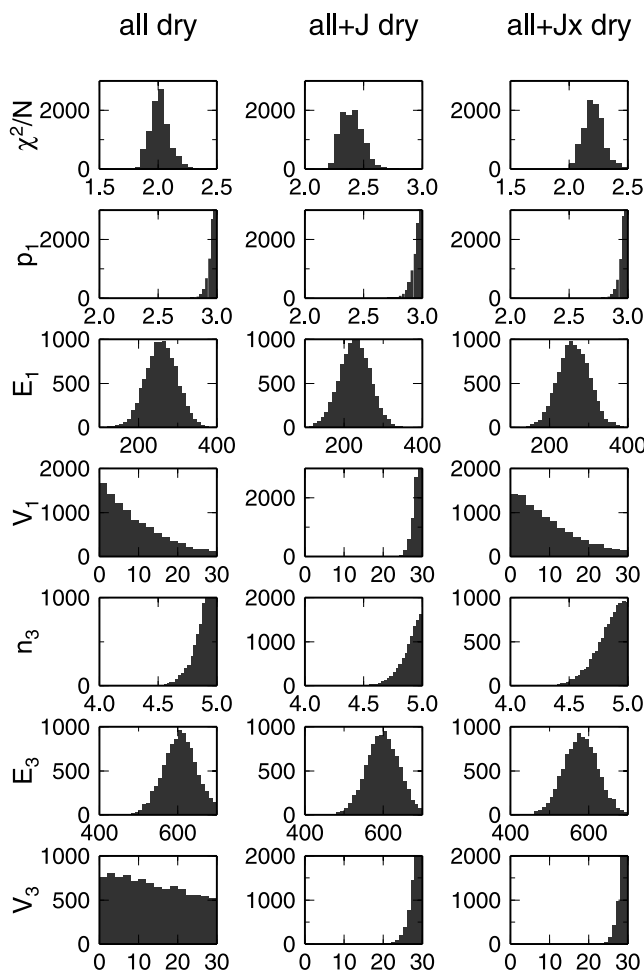


Figure 8. Histograms of 10^4 MCMC solutions from supplementary simulations with additional high-pressure data (right two panels). “all+J dry” denotes the simulation in which the reported fine grain sizes for the JK01 data are used as is. The grain sizes are increased by a factor of 10 in the simulation “all+Jx dry”. The histogram for the standard simulation is also shown for comparison (left panel).

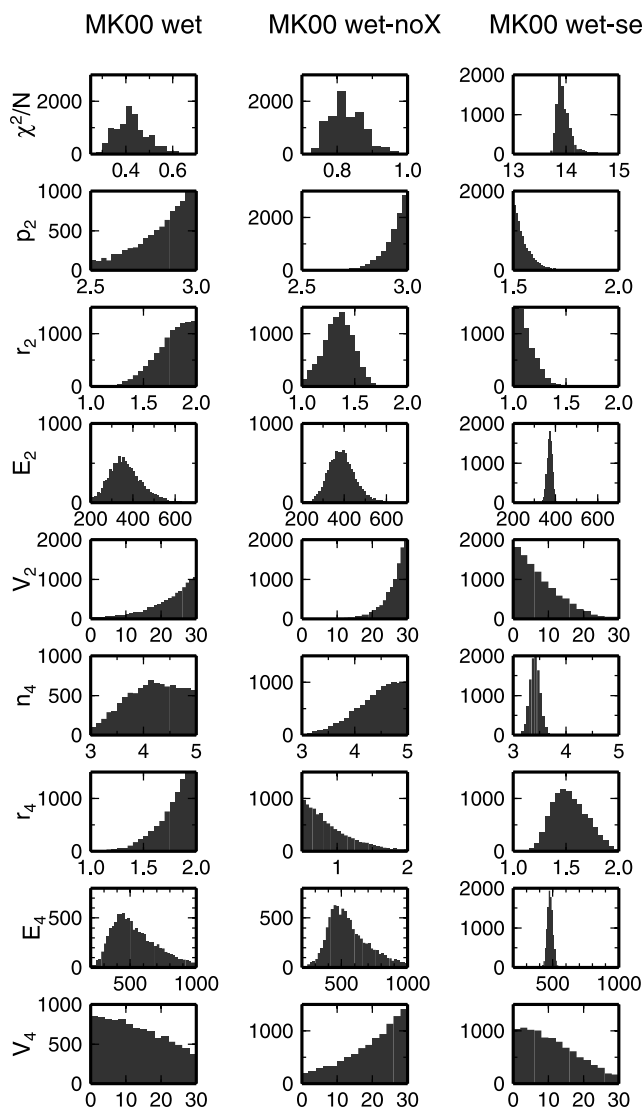


Figure 9. Histograms of 10^4 MCMC solutions with the wet MK00 data: (left) the standard simulation, (middle) the simulation with no inter-run biases, and (right) the simulation with neglecting $\text{rvar}\{i, s_i^m\}$.

tions, using only the MK00 data (Figure 9). The importance of inter-run biases for these wet data is clear from Figure 1, and in fact whether biases are modeled or not resulted in very different estimates for some parameters, most notably the water-content exponents r_2 and r_4 . A conventional value for the water-content exponent is ~ 1 , for both diffusion and dislocation creeps, but our standard simulation (“MK00 wet”) indicates that these exponents are more likely to be ~ 2 . The inversion with simplified error (“-se”) once again demonstrates that accounting for all of experimental uncertainties is essential to properly estimate flow-law parameters as well as their uncertainties.

[55] The high water-content exponents may be surprising, but as shown later, they turn out to be persistent even with larger data sets. To understand the cause of discrepancy with previous estimates, we focused on the following four runs from MK00: PI-107, PI-184, PI-569, and PI-204 (Figure 10). All of these runs were conducted at 1523 K but at different

pressures (thus different water contents); PI-107 was at 0.3 GPa, PI-184 at 0.1 GPa, and PI-569 at 0.45 GPa. These three runs are what *Mei and Kohlstedt* [2000a] used to determine the exponent r_2 . PI-204 started at 0.1 GPa, and the pressure was gradually increased to 0.3 GPa. PI-204 was conducted with a nearly constant stress ($\sigma_1 - \sigma_3 \sim 28$ MPa, or $\sigma_{II} \sim 16$ MPa), so we chose the reference stress of 16 MPa. Using the estimated flow law, we first normalized these four runs to the reference stress (Figure 10a), then corrected for different grain sizes (Figure 10b), and finally corrected for the pressure effect using the estimated activation volumes (Figure 10c). In Figure 10c, the trend exhibited by PI-204 is clearly much steeper than $r_2 = 1$ and closer to $r_2 = 2$, whereas the trend composed by other three runs may be close to $r_2 = 1$. It is thus not surprising that *Mei and Kohlstedt* [2000a] estimated r_2 to be ~ 1 , but their estimation method implicitly assumes that inter-run biases are negligible. As can be seen from Figure 1, this is an unwarranted assumption especially for the wet deformation data. When estimated inter-run biases were applied, all runs became consistent with $r_2 \sim 2$ (Figure 10d). Note that the biases were not determined just to align the three runs with PI-204. In our MCMC simulation, inter-run biases are estimated to make the entire data set as internally consistent as possible, by simultaneously taking into account the variation of strain rate with respect to temperature, pressure, grain size, stress, and water content. Our treatment of inter-run bias is, however, still preliminary (i.e., assumed to be constant during an experimental run), and a more careful experimental study is essential to finalize our estimate on the water-content exponent.

[56] Adding more experimental runs from KPF86 and J06 generally resulted in reducing the uncertainty of flow-law parameters (“MK + K wet” and “all wet” in Figure 11). The only exception is the grain-size exponent p_2 . With all relevant runs, the stress exponent n_4 is now defined around 3.6, the water-content exponents are both likely to be ~ 2 , and the activation volume for dislocation creep (V_4) appears to be well constrained to be $< \sim 10$ cm³ mol⁻¹. Our inference on activation energies was not noticeably improved, and they remain relatively broadly defined as $E_2 = 390 \pm 50$ kJ mol⁻¹ and $E_4 = 520 \pm 100$ kJ mol⁻¹. Similarly, the activation volume for diffusion creep is broadly defined to be $> \sim 15$ cm³ mol⁻¹. Inter-run biases (with respect to MK00’s PI-107) estimated by the standard simulation with all wet data are shown in Figure 7b.

[57] By extending the a priori bounds as we did in the dry case ($\max(p) = 5$, $\max(n) = 6$, $\max(r) = 4$, and $\max(V) = 60$), one can see that some of these parameters, especially those for dislocation creep, cannot be stably estimated without such bounds (Figure 11, right panel). Some parameters (p_2 and n_4) exhibit bimodal distributions, indicating that this minimization problem has at least two significant local minima. Compared to dry deformation data, wet deformation data have an additional uncertainty due to water concentration, which provides an extra space for parameter uncertainties. Whereas diffusion creep parameters are still estimated reasonably (i.e., similar to the standard simulation result) except for the activation volume, dislocation creep is not. Thus regularizing our highly nonlinear inversion is more important for this wet case.

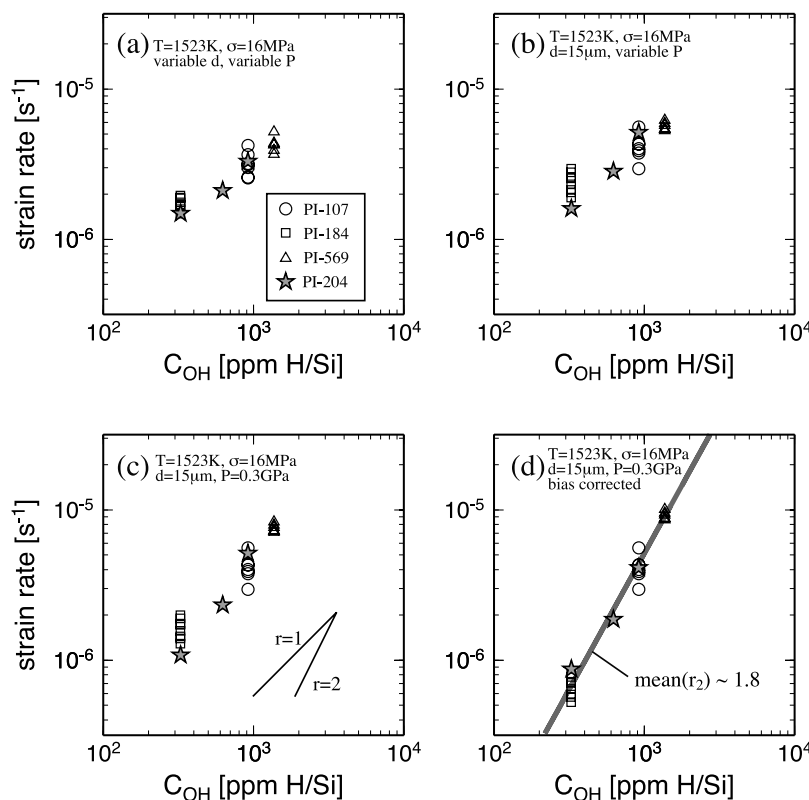


Figure 10. Wet experimental runs from MK00 (PI-107, PI-184, PI-569, and PI-204) are plotted in the water content vs. strain rate space with stepwise normalization. All runs are conducted at 1523 K. (a) Corrected for variations in stress (normalized to $\sigma = 16$ MPa). (b) Corrected for grain size effect (normalized to $d = 15 \mu\text{m}$). (c) Corrected for pressure effect (normalized to $P = 0.3$ GPa). (d) Corrected for inter-run biases.

4.3. Testing Convergence and Consistency

[58] We take the results from the standard simulations with all dry and wet data (shown as “all dry” in Figure 6 and “all wet” in Figure 6) collectively as our best estimate on the olivine flow law. We then computed two different diagnostics to see whether these simulations have successfully converged. One is the autocorrelation function (Figure 12), which is the correlation between a given Markov chain shifted by a certain number of steps (called ‘lag’). The autocorrelation of a good Markov chain decreases quickly with an increasing lag. Figure 12 shows that the autocorrelation of our MCMC simulation becomes virtually zero within a lag of ~ 100 – 200 for most of model parameters. Activation energies require longer lags (~ 600). This is because, compared to other parameters, it is more difficult to change them randomly; even a small change in activation energy could affect the cost function considerably. Because we sampled every 10^3 models, this behavior of autocorrelation indicates that sampled solutions are very close to be statistically independent.

[59] The second diagnostic is a comparison between ten parallel runs (Figure 13). We calculated the mean and standard deviation of model parameters for each MCMC run, and as Figure 13 shows, the results of those parallel runs are almost indistinguishable from each other. We are thus reasonably confident in having explored the entire model space, and the distribution of our MCMC solutions

should correspond closely to the a posteriori probability distribution $\rho(\mathbf{m})$.

[60] As noted in section 2.1, we assumed that the wet deformation data are characterized by high enough water concentrations, so they can be modeled solely by the wet flow law. To test this assumption, we compared the wet deformation data with those predicted by the dry flow law at the same temperature, pressure, stress, and grain size conditions (Figure 14). Except for two data points, the observed strain rates are larger than or equal to the predicted ones, supporting our assumption. Note that quite a few data plot on the dry prediction, and they are all from experiments conducted at 0.1 GPa (i.e., low water content). That is, these low-pressure wet experiments were conducted in the vicinity of a dry-to-wet transition. As far as our assumption for this transition (equation (7)) holds, this does not pose any problem; deformation at this transition can be modeled either by the dry or wet flow law, and it is modeled by the wet flow law in our strategy. If instead equation (6) is found to be more appropriate, however, a greater care would be required to model these low-pressure data.

[61] Our MCMC simulations have resulted in not only quantifying the uncertainty of flow-law parameters but also revising some of parameters themselves. Our statistical framework as summarized by equation (9) is by far the most comprehensive one, and these findings are the product of interpreting all of existing high-quality deformation data

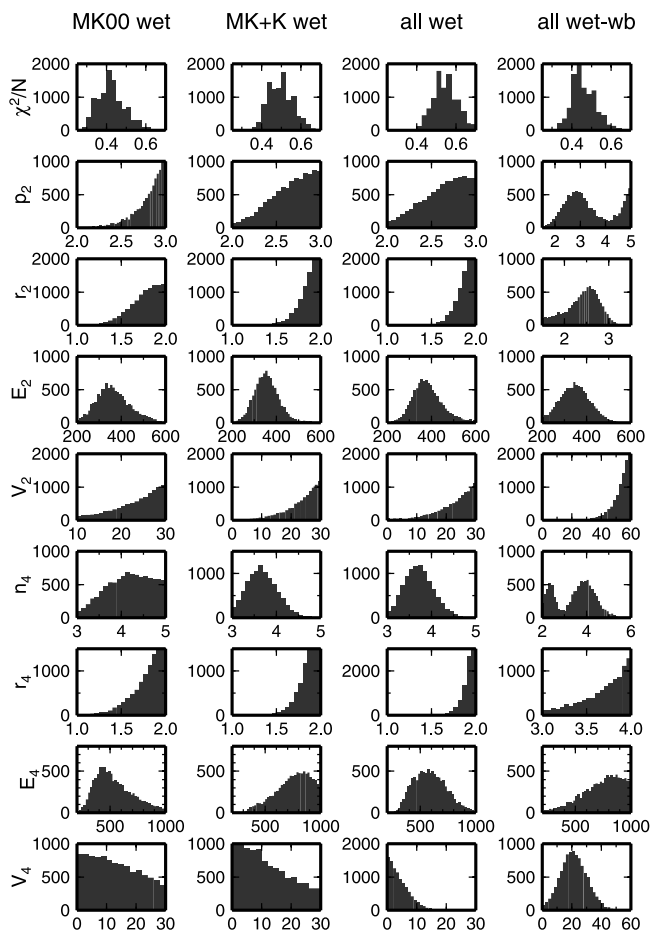


Figure 11. Histograms of 10^4 MCMC solutions from four different simulations with wet experimental runs. “MK00 wet” is the same as shown in the left panel of Figure 9. “MK+K dry” is the simulation with the MK00 and KPF86 data. “all wet” and “all wet-wb” are the simulations with all of wet experimental runs with the standard and extended a priori bounds, respectively.

in terms of the composite flow law (equation (5)), by exploring the entire model space. Perhaps the optimal way to confirm our results is to conduct deformation experiments over wider temperature and pressure ranges, which should become possible in future.

[62] In Figures 15 and 16, we compare ‘observed’ strain rates with the prediction of the estimated flow law in a variety of different ways. Note that the ‘observed’ strain rates in these plots are already modified by the estimated flow law. For example, when we want to plot data in the grain-size versus strain rate space at a given reference state in order to visualize grain-size sensitivity (e.g., Figures 15a and 15b), data must be normalized to the reference state by correcting differences in temperature, pressure, stress, and water content, for which we need to use a flow law. This sort of visualization or data normalization, therefore, can be done only after all of relevant flow-law parameters are determined. If this guideline is not followed and if some parameters are instead assumed for normalizing data, such normalization might lead to an erroneous estimate on other

parameters. In these comparison plots, we show both dry and wet cases, or low-stress and high-stress cases, or the combination of both. The prediction of the flow law as well as the contributions of relevant creep mechanisms are shown, and these plots support that the new flow law is consistent with experimental data over a range of experimental conditions. Moreover, these plots suggest that simultaneously inverting for both diffusion and dislocation creeps is important not only for the stress exponent but also for the activation energies and volumes. On the other hand, simultaneously inverting for both dry and wet flow laws is not essential as long as equation (7) is correct. If we parameterize the flow law differently, however, we would have a different situation, so it is important to develop a better theoretical model for this transition.

4.4. Statistical Representation of Olivine Rheology

[63] The 10^4 MCMC solutions produced in the previous section are distributed over the 8-dimensional model space for the dry flow law and the 10-dimensional space for the wet flow law, and it is desirable to find a more compact representation for the model subspace that encompasses these solutions. To this end, we conducted the principal component analysis (PCA), which transforms the original model parameters into a set of new, uncorrelated variables (called principal components) in order of decreasing significance [e.g., *Gershenfeld*, 1998]. The significance of a particular principal component is measured by its eigenvalue, and Figure 17 shows the eigenvalues of all principal components normalized by the largest one. For both dry and wet cases, the last two components have eigenvalues smaller than 10% of the largest one, indicating that the true dimension of the model subspace is approximately 6 (dry) and 8 (wet), respectively. In other words, among 8 (dry) or 10 (wet) flow-law parameters, two model parameters are not linearly independent from other parameters, so any set of two parameters can be expressed by a linear combination of the other parameters. This result may be apparent from how the scaling constants A_i are constrained by data fit (Appendix B). Because we cannot reduce the dimensionality of the model subspace further, the uncertainty of flow-law parameters other than the scaling constants do not correlate notably to each other. That is, one can choose values for p_i , r_i , n_i , E_i , and V_i randomly from their a posteriori distributions (“all dry” in Figure 6 and “all wet” in Figure 11), and the combination of these random picks should still be able to explain experimental data as long as A_i (or B_i) are chosen properly.

[64] Our first task was therefore to describe the a posteriori distributions of these 14 parameters. As some of these distributions deviate considerably from the Gaussian distribution, we chose to use the median and interquartile range (IQR). IQR is based on quartiles and is a stable measure of statistical dispersion. The first quartile (Q_1) is the value that cuts off the lowest 25% of data, the second quartile (Q_2 or median) cuts data in half, and the third quartile (Q_3) cuts off the highest 25%. IQR is defined as $Q_3 - Q_1$. Table 2 summarizes the median, Q_1 , and IQR for the 14 flow-law parameters. By doing this, we are essentially neglecting the lower and upper 25% of the probability distribution, which is our compromise for a compact statistical description.

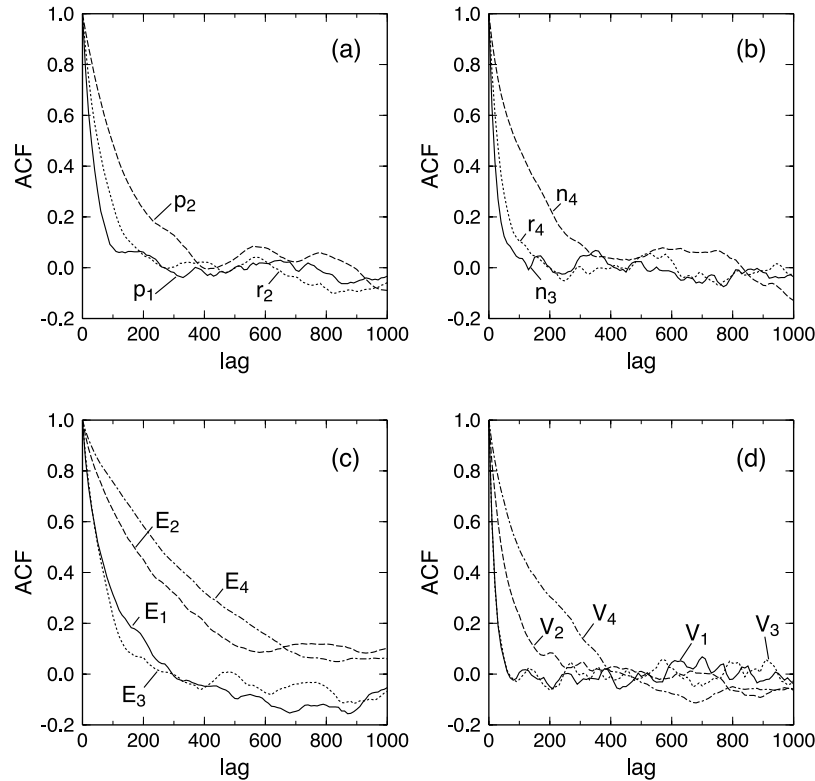


Figure 12. Autocorrelation function (ACF) for representative MCMC runs with all dry and wet experimental runs. (a) Grain-size exponents (p_1 and p_2) and water-content exponent for diffusion creep (r_2). (b) Stress exponents (n_3 and n_4) and water-content exponent for dislocation creep (r_4). (c) Activation energies ($E_1 - E_4$). (d) Activation volumes ($V_1 - V_4$).

[65] The normalized scaling constants B_i were then modeled by a linear combination of these parameters q_k :

$$B_i = a_{0,i} + \sum_{k=1}^{14} a_{k,i} \left(\frac{q_k - q_k^m}{\Delta q_k} \right), \quad (22)$$

where q_k^m and Δq_k denote the median and IQR of q_k , respectively, and $a_{k,i}$ are the best fit coefficients determined by linear regression with the MCMC solutions. These coefficients are also listed in Table 2, completing our statistical representation of the flow law for olivine aggregates.

[66] Note that we used two runs from MK00 (PI-181 for dry runs and PI-107 for wet runs) as a reference to define the biases of other experimental runs, and if we use a different run as a reference, the scaling constants must be adjusted up or down uniformly. Estimated inter-run biases are distributed in a random fashion around the chosen reference (Figure 7), and this type of uncertainty in the scaling constants is probably about a factor of ~ 2 .

[67] As we emphasized in Introduction, it is important to appreciate the limitation of our knowledge and explore its consequences in geodynamical modeling. Using just one particular flow law is not sufficient. There are a number of equally valid but different flow laws with different geodynamical consequences. Model predictions with composite mantle rheology may be called robust only when they are

based on common features among those different results. Generating a number of flow laws is straightforward with Table 2. For each of the 14 flow-law parameters, pick a number randomly from the interval bounded by Q_1 and Q_3 ($=Q_1 + \text{IQR}$), and then calculate A_i using equations (22) and (20). This provides all parameters needed by the flow law of equations (1)–(4).

[68] Profiles of effective viscosity ($\equiv \sigma/\dot{\epsilon}$) for a few illustrative cases were calculated in two different ways and are compared in Figure 18. One was calculated directly from 10^4 MCMC solutions, and the other from 100 randomly generated flow laws using Table 2. For the uncertainty of predicted viscosity profiles, one standard deviation is used for the former whereas the total range (i.e., from the minimum viscosity to the maximum one at any given depth) is used for the latter. As seen in Figure 18, these two different approaches yield similar predictions both for the ridge and cold geotherms. Taking the total range instead of one standard deviation appears to compensate well the neglect of the lower and upper 25% of the a posteriori distributions when summarizing our MCMC simulations in the form of Table 2, though uncertainties associated with the dry diffusion creep (mostly originating in V_1) tend to be underestimated by the statistical representation. Figure 18 confirms that mantle viscosity can be affected substantially by a change in the water content [Karato, 1986; Hirth and Kohlstedt, 1996], and also suggests that this effect of water

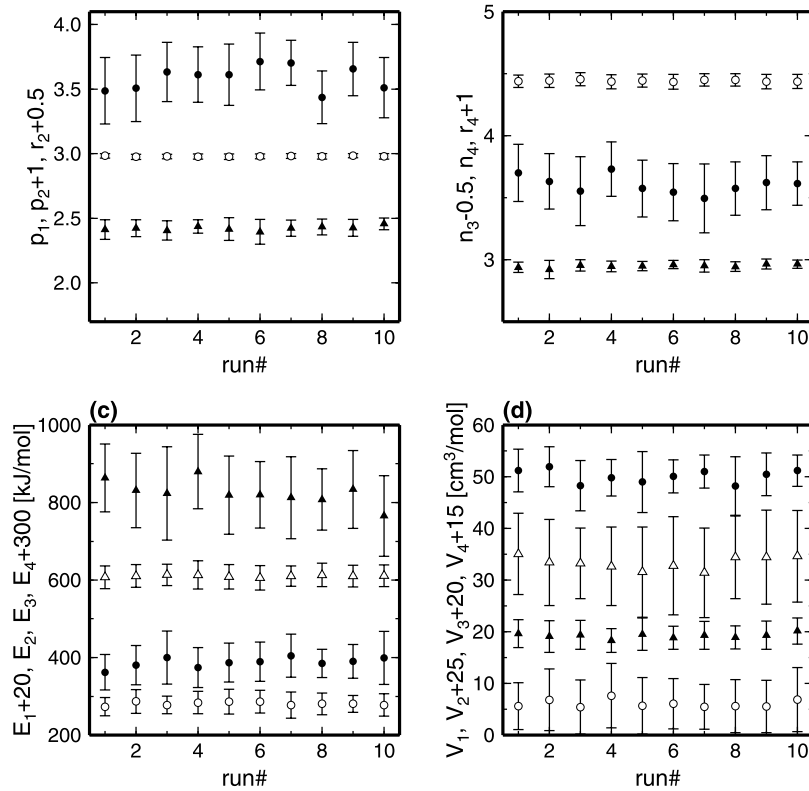


Figure 13. Comparison of ten parallel MCMC runs. Some parameters are shifted up or down for clarity, as indicated by the label on the vertical axis. Error bars indicate one standard deviation. (a) p_1 (open circle), p_2 (solid circle), and r_2 (solid triangle). (b) n_3 (open circle), n_4 (solid circle), and r_4 (solid triangle). (c) E_1 (open circle), E_2 (solid circle), E_3 (open triangle), and E_4 (solid triangle). (d) V_1 (open circle), V_2 (solid circle), V_3 (open triangle), and V_4 (solid triangle).

content is persistent in the dislocation creep regime throughout the upper mantle.

5. Discussion and Conclusion

[69] Table 3 compares the flow-law parameters estimated in this study with previous compilations by *Karato and Wu* [1993] and *Hirth and Kohlstedt* [2003]. We first note that the scaling constants A_i can vary easily by a few orders of magnitude for a small change in activation energies E_i , so comparison in terms of the scaling constants is not very informative. As already described, this study conforms to the previous studies for some parameters such as p_1 , p_2 , n_4 , V_1 , and V_3 , but is substantially different for others, most notably n_3 , r_2 , r_4 , and V_2 . Differences in activation energies may not seem to be large because they have always been associated with relatively large uncertainties, but this study is the first to quantify their most likely values and uncertainties by the fully global inversion. The activation energy for dry diffusion creep (E_1) is slightly lower than conventionally thought, that for wet diffusion creep (E_2) is slightly higher and, more importantly, E_2 is greater than E_1 . The activation energies for dry and wet dislocation creeps (E_3 and E_4) are both higher than previous estimates by 50–100 kJ mol⁻¹. Note that Table 3 is shown here merely for the sake of comparison. We emphasize the importance of using the more complete statistical representation summarized in Table 2.

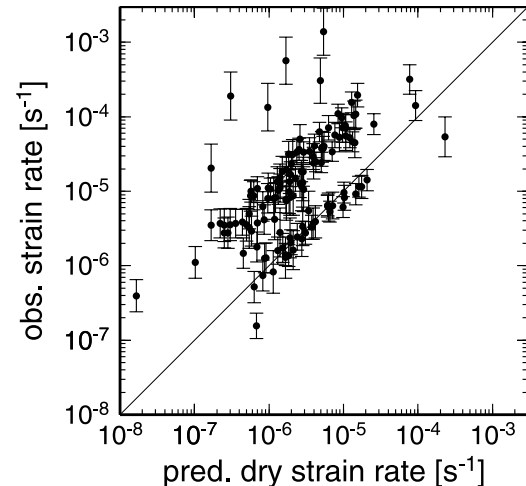


Figure 14. Strain rates observed at wet experimental runs are compared with those predicted by the dry flow law at the same temperature, pressure, stress, and grain size conditions (based on the “all dry” simulation result). The error bar of strain rate includes all other experimental uncertainties. Bias correction is also applied. If our assumption behind equation (7) is correct, all data should be plotted on or above the diagonal.

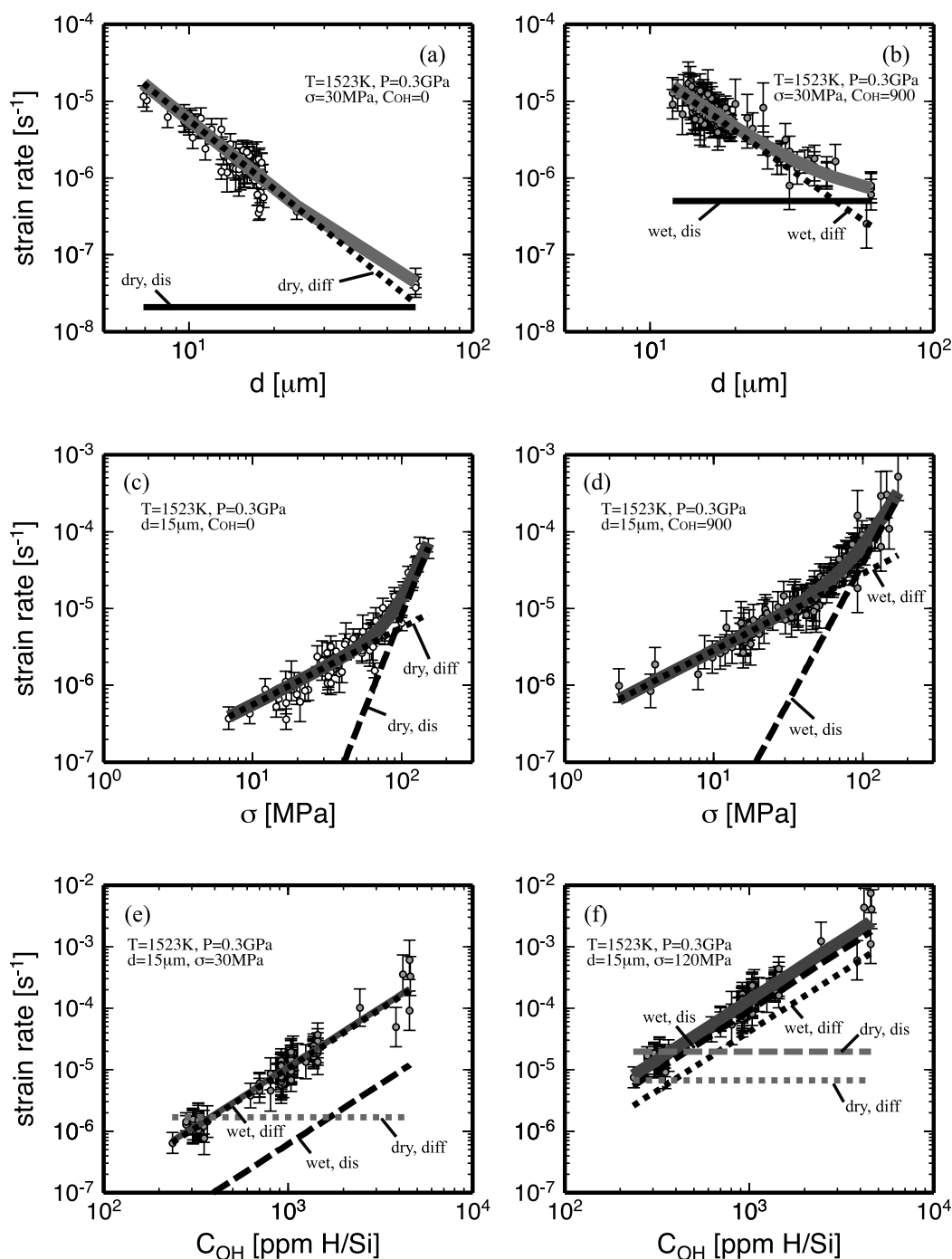


Figure 15. Comparison of experimental data (circles) with the estimated flow law (thick gray curves) in (a,b) grain size versus strain rate, (c,d) stress versus strain rate, and (e,f) water content vs. strain rate. Error bar includes all experimental uncertainties and bias correction is applied. Reference states are given in the plots. Open and gray circles denote dry and wet experiments, respectively. In Figures 15e and 15f, the predictions by the dry deformation mechanisms are shown to indicate the threshold water content for the dry-to-wet transition (~ 300 ppm H/Si).

[70] In order to estimate a composite flow law, we combined different experimental runs and even different experimental studies, and this approach is markedly different from a more conventional approach, in which flow-law parameters are estimated sequentially from more restricted data sets. For example, activation energy has

often been estimated from a single experimental run, in which temperature is varied but other variables are kept constant [e.g., *Mei and Kohlstedt, 2000a*]. As our analysis suggests, however, the contribution of diffusion creep is not negligible even at high stresses (Figures 16b and 16d), so an estimate can be made only for an ‘apparent’

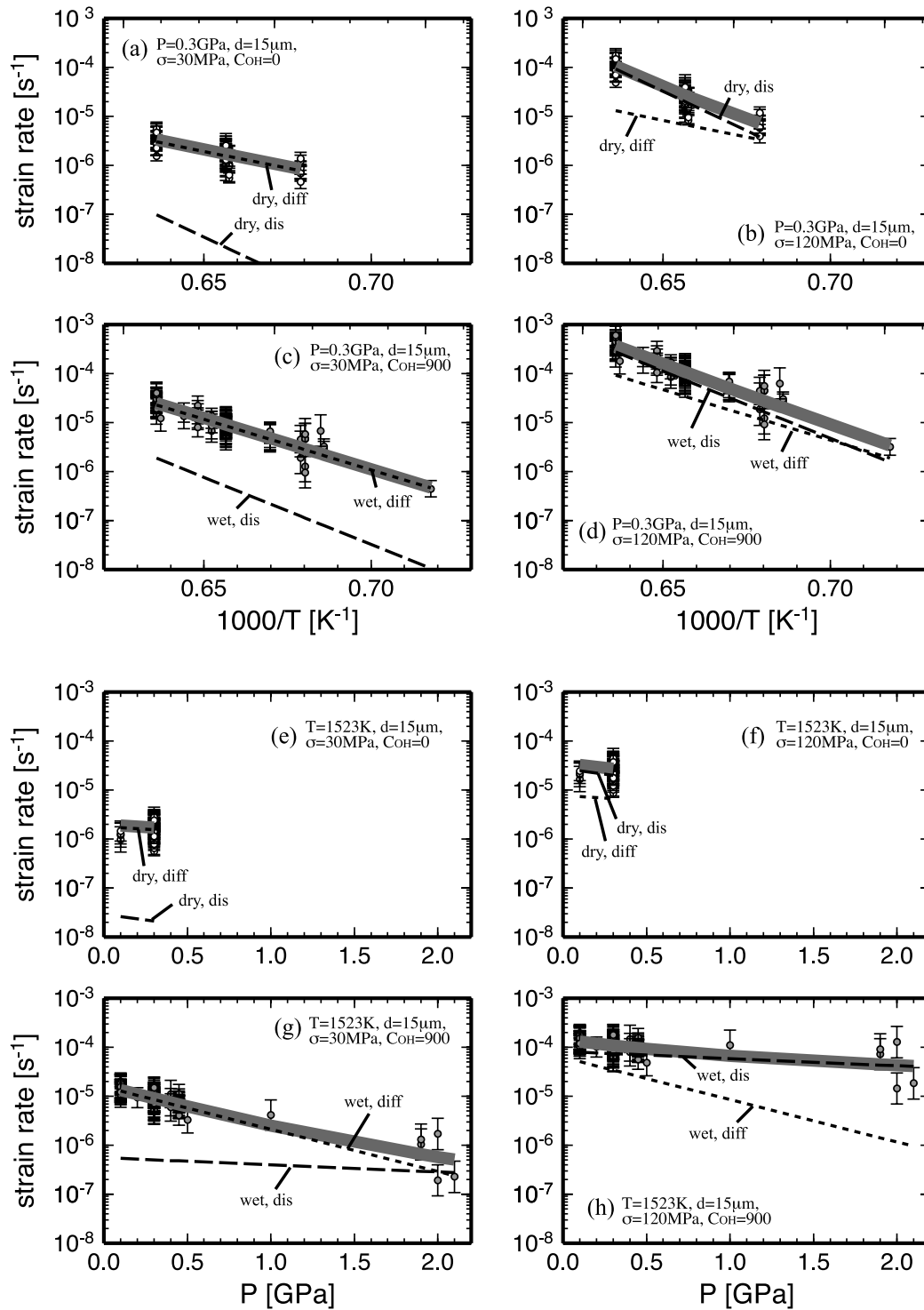


Figure 16. Comparison of experimental data (circles) with the estimated flow law (thick gray curves) in (a–d) inverse temperature versus strain rate and (e–h) pressure versus strain rate. Four cases are shown: dry diffusion regime (a,e), dry dislocation regime (b, f), wet diffusion regime (c, g), and wet dislocation regime (d, h). The meaning of symbols and curves are the same as in Figure 15.

activation energy, which by itself is not very useful. One may wish to subtract the contribution of diffusion creep beforehand to estimate the activation energy of dislocation creep, but the flow law of diffusion creep has some finite uncertainty, which should contribute to the uncertainty of

the estimated activation energy. Handling error propagation would thus be quite cumbersome in this sequential approach. By inverting for a composite flow law simultaneously, we can estimate separately the activation energies of different creep mechanisms, with the interrelation of

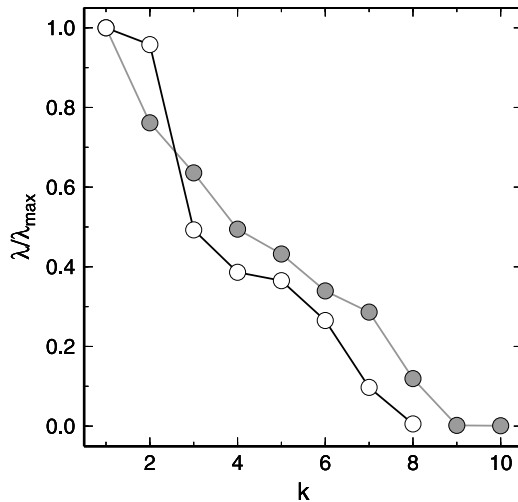


Figure 17. Eigenvalues corresponding to principal components for 8 (dry, open circles) and 10 (wet, gray circles) flow-law parameters, normalized by the largest eigenvalue.

parameter uncertainty automatically taken care of. The conventional approach may appear to be simpler or better, but it is actually prone to yield misleading results when the majority of data lie near the transition from diffusion to dislocation creep, which is exactly the case for existing data on olivine rheology. Of course, merging different kinds of experimental data has to be done carefully. Our approach with inter-run bias not only estimates all of flow-law parameters simultaneously but also constructs the most self-consistent data set at the same time by honoring ‘trends’ exhibited by individual runs (e.g., apparent activation energy in a temperature-stepping experiment).

[71] The exponents p_i , n_i , and r_i as well as activation parameters E_i and V_i are usually interpreted in terms of relevant microscopic processes, so our results should also affect such an interpretation. Our preferred flow law is subject to future revision as new experimental results become available, but our statistical framework will remain useful to assimilate such new data and update the experimental bounds. Figure 18 illustrates that although some

parameters remain poorly constrained, we can still draw some robust conclusions on the rheological structure of the upper mantle such as the large effects of dehydration [e.g., Karato, 1986; Hirth and Kohlstedt, 1996]. The asthenosphere is believed to contain a trace amount of water (~ 800 ppm H/Si in olivine [Hirth and Kohlstedt, 1996]), and wet dislocation creep could be the dominant deformation mechanism throughout the upper mantle. At shallow depths ($< \sim 70$ km), oceanic mantle is dry due to dehydration upon partial melting beneath mid-ocean ridges, but at these depths, dry rheological properties are reasonably well constrained because the pressure effects are small.

[72] When running a numerical model with complex rheology, it is important to map the uncertainty of an assumed rheology to model uncertainty. Otherwise, it would be unclear how much we could rely on the outcome of such numerical modeling. This study should help to address this issue for upper mantle dynamics. Even though some flow-law parameters of olivine rheology still have large uncertainties, other parameters are reasonably well defined. By conducting numerical modeling with a large number of possible flow laws, we should be able to identify which aspects of model results are robust and which suffer from flow-law uncertainties, and this sort of exercise could motivate future experimental studies. Statistics is an important interface between experimental rock mechanics and theoretical geodynamics.

[73] Our approach is based on (1) modeling experimental data by a composite flow law with all of experimental uncertainties taken into account, and (2) exploring the model parameter space extensively by efficient MCMC sampling. The difference between our method and the traditional global inversion method of Sotin and Poirier [1984] is similar to the difference between a general theoretical framework proposed by Tarantola and Valette [1982a] and a more restricted case studied in depth by Tarantola and Valette [1982b]. The method of Sotin and Poirier [1984] is based on the latter, and implementing a more general method is computationally more expensive. MCMC simulations indeed require a very large number of iterations, but it can be easily conducted with reasonable computing resources available today. We emphasize, how-

Table 2. Statistical Representation of Olivine Flow Law E_i are in kJ mol^{-1} and V_i are in $\text{cm}^3 \text{mol}^{-1}$

Parameters ^a	Median	Q_1^b	IQR ^c	$a_{k,1}$	$a_{k,2}$	$a_{k,3}$	$a_{k,4}$
($k = 0$)				-3.7478	-9.0248	-14.9414	-17.5794
p_1	2.97	2.95	0.04	0.0472	0	-0.0005	0
E_1	258	232	54	0.0052	0	-0.0010	0
V_1	7.2	3.1	10	-0.0009	0	0.0005	0
p_2	2.66	2.45	0.39	0	0.4903	0	0.0022
r_2	1.91	1.84	0.12	0	-0.3564	0	-0.0022
E_2	377	337	88	0	-0.0143	0	-0.0101
V_2	24.4	19.3	8.3	0	-0.0159	0	-0.0030
n_3	4.92	4.86	0.11	0.0020	0	-0.2190	0
E_3	607	578	58	0.0053	0	-0.0082	0
V_3	13.3	6.4	14.5	0.0009	0	-0.0020	0
n_4	3.70	3.48	0.45	0	0.0241	0	-0.8854
r_4	1.95	1.90	0.08	0	-0.0016	0	-0.2328
E_4	578	476	211	0	0.0005	0	0.0851
V_4	3.6	1.6	4.7	0	-0.0022	0	0.0003

^a p_1 corresponds to $k = 1$, E_1 to $k = 2$, and so on.

^bFirst quartile.

^cInterquartile range.

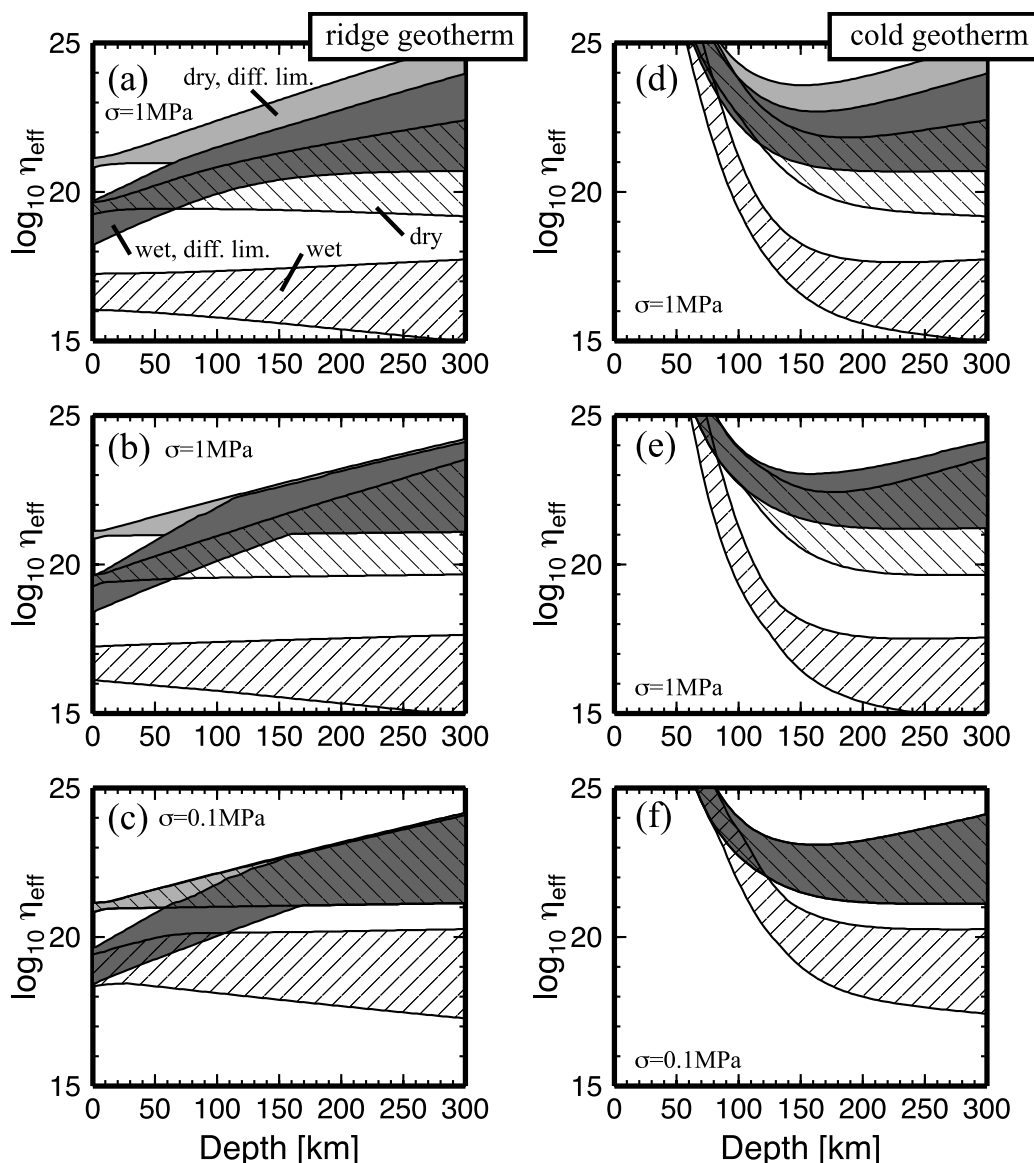


Figure 18. Effective viscosity profiles predicted for the upper 300 km of Earth. The water content is fixed to 0 and 800 ppm H/Si, respectively, for dry and wet cases. Grain size is 10 mm. For a ridge geotherm (left panel), the potential temperature of 1623 K is used with the adiabatic gradient of 0.5 K km^{-1} . A cold geotherm (right) is for 100-Ma-old oceanic mantle as predicted by a half-space cooling model with the thermal diffusivity of $10^{-6} \text{ m}^2 \text{ s}^{-1}$. (a,d) Effective viscosity and its uncertainty based on 10^4 MCMC solutions. σ is assumed to be 1 MPa. (b,e) Same as Figures 18a, 18d but based on 100 random flow laws generated from Table 2 (c,f) Same as Figures 18b, 18e but with σ of 0.1 MPa. Diffusion limit cases consider only diffusion creep mechanisms (equations (1) and (2)). Note that, for the uncertainty of viscosity profiles, one standard deviation is used for Figures 18a and 18d, and the total range from the minimum viscosity to the maximum one is used in other cases.

ever, that our statistical framework is not complete even though it is by far the most comprehensive one. For example, the parameterization of inter-run bias is kept simple because a more elaborate treatment requires more information on experimental details, which may not always be available. Moreover, how we should model a dry-to-wet transition in a general flow law may be subject to discussion, and if we could confidently propose a more appropriate functional form on the basis of microscopic mechanisms, it would also improve the reliability of inversion results.

[74] The present analysis has shown that the existing experimental data and their analyses contain major limitations. In particular, the rheological data under wet conditions show a large scatter indicating that poorly controlled ‘hidden’ parameters have important influence on rheological properties. Among others, the degree to which a sample is saturated with water during an experiment needs to be carefully analyzed in order to obtain results that can be applied to geodynamic modeling. Also, the influence of pressure is still very poorly constrained, mainly because of the paucity of quantitative data under high pressures. In

Table 3. Comparison With Previous Compilations E_i are in kJ mol⁻¹ and V_i are in cm³ mol⁻¹

Mechanism	Parameters	Karato	Hirth and	This
		and Wu [1993]	Kohlstedt [2003]	Study ^a
Dry diffusion	A_1	10 ^{9.38}	10 ^{9.18}	10 ^{5.25±0.03}
	p_1	2.5	3	2.98 ± 0.02
	E_1	300	375 ± 50	261 ± 28
	V_1	6	2–10	6 ± 5
Wet diffusion	A_2	10 ^{5.15}	10 ^{6.0}	10 ^{4.32±0.38}
	p_2	2.5	3	2.56 ± 0.24
	r_2	-	1	1.93 ± 0.07
	E_2	240	335 ± 75	387 ± 53
Dry dislocation	V_2	5	4	25 ± 4
	A_3	10 ^{-1.22}	10 ^{5.04}	10 ^{6.09±0.11}
	n_3	3.5	3.5 ± 0.3	4.94 ± 0.05
	E_3	540	530 ± 4	610 ± 30
Wet dislocation	V_3	15–25	14–27	13 ± 8
	A_4	10 ^{1.0}	10 ^{1.95}	10 ^{0.6±0.5}
	n_4	3.0	3.5 ± 0.3	3.60 ± 0.24
	r_4	-	1.2	1.95 ± 0.05
	E_4	430	480 ± 40	523 ± 100
	V_4	10–20	11	4 ± 3

^aListed are mean values with one standard deviation. The standard deviations of A_i 's are from those of B_i 's only and do not include the uncertainty due to activation energy and volume.

addition, the influence of plastic anisotropy has not been addressed in any detail yet. We conclude that a detailed statistical analysis on uncertainties as well as better-controlled experiments under wet and high-pressure conditions are imperative for a better understanding of the rheological properties of Earth's mantle.

Appendix A: Relative Variance due to Experimental Variables

[75] When we model data, y_i , as a linear function of x , i.e.,

$$y_i = a + bx_i, \quad (\text{A1})$$

and when both x_i and y_i are subject to uncertainty, the misfit between the data and the model prediction should be measured as [e.g., *Reed*, 1989]:

$$\chi^2(a, b) = \sum_i \frac{(y_i - a - bx_i)^2}{\text{var}\{y_i\} + b^2 \text{var}\{x_i\}}, \quad (\text{A2})$$

because

$$\text{var}\{y_i - a - bx_i\} = \text{var}\{y_i\} + b^2 \text{var}\{x_i\}. \quad (\text{A3})$$

[76] Similarly, to model observed deformation data $\dot{\epsilon}_{\text{obs}}$ with equation (8) in the logarithmic scale, we need to consider the following:

$$\text{var}\left\{\log \dot{\epsilon}^j - \log \sum_i \dot{\epsilon}_i(s_i^j) - X^j\right\} \approx \frac{\text{var}\{\dot{\epsilon}^j\}}{(\dot{\epsilon}^j)^2} + \frac{\text{var}\left\{\sum_i \dot{\epsilon}_i(s_i^j)\right\}}{\left(\sum_i \dot{\epsilon}_i(s_i^j)\right)^2}, \quad (\text{A4})$$

where the first-order Taylor expansion is employed for approximation and $\text{var}\{X^j\}$ is zero because X^j is a model parameter and not an observable. The first term is $\text{rvar}\{\dot{\epsilon}^j\}$, and the second term can be further approximated with the Taylor expansion as:

$$\frac{\text{var}\left\{\sum_i \dot{\epsilon}_i(s_i^j)\right\}}{\left(\sum_i \dot{\epsilon}_i(s_i^j)\right)^2} \approx \sum_i \text{rvar}\{i, s_i^j\}, \quad (\text{A5})$$

where $\text{rvar}\{i, s_i^j\}$ depends on the form of the i -th flow law. All the flow laws under consideration (equations (1)–(4)) can be expressed in the following general form:

$$\dot{\epsilon}_k = A_k d^{-p_k} \sigma^{n_k} C_{OH}^{r_k} \exp\left(-\frac{E_k + pV_k}{RT}\right), \quad (\text{A6})$$

for which we have

$$\text{rvar}\{k, s_i^j\} = \left(\frac{\dot{\epsilon}_k^j}{\sum_i \dot{\epsilon}_i^j}\right)^2 \left(p_k^2 \frac{\text{var}\{d^j\}}{(d^j)^2} + n_k^2 \frac{\text{var}\{\sigma^j\}}{(\sigma^j)^2} + r_k^2 \frac{\text{var}\{C_{OH}^j\}}{(C_{OH}^j)^2} + \left(\frac{V_k}{RT^j}\right)^2 \text{var}\{p^j\} + \left(\frac{E_k + p^j V_k}{R(T^j)^2}\right)^2 \text{var}\{T^j\} \right). \quad (\text{A7})$$

Appendix B: How to Randomize Scaling Constants in MCMC

[77] The flow law (equation (5)) is linear in A_i , i.e., it may be expressed as

$$\dot{\epsilon}^j = \sum_{i=1}^2 f_i^j A_i, \quad (\text{B1})$$

where f_i^j represent the parts that are completely determined once all flow-law parameters other than A_i are specified. When the number of data is larger than 2, this constitutes an overdetermined linear system, which can be solved for A_i by the method of least squares. However, both $\dot{\epsilon}^j$ and f_i^j vary over many orders of magnitudes, so a direct application of least squares to equation (B1) does not result in a reasonable data fit in the logarithmic scale. The logarithmic version of equation (B1) is, however, not linear in A_i . It can be solved by a more time-consuming nonlinear inversion, but because estimating ‘best fit’ A_i is a part of each Markov step (which has to be iterated over $>10^6$ times), it is better to use a quicker alternative. We find that the following successive rescaling works reasonably well. First, we scale by the strain rate error as:

$$b_i = \sum_{i=1}^2 F_i^j A_i, \quad (\text{B2})$$

where $b_i = \dot{\epsilon}^j / \sqrt{\text{var}\{\dot{\epsilon}^j\}}$ and $F_i^j = f_i^j / \sqrt{\text{var}\{\dot{\epsilon}^j\}}$. It is then scaled as:

$$b_i = \sum_{i=1}^2 G_i^j C_i, \quad (\text{B3})$$

where $G_i^j = F_i^j/\alpha_i$, $C_i = A_i \alpha_i$, and

$$\alpha_i = \exp\left(\frac{\sum_{j=1}^N \log F_i^j}{N}\right), \quad (\text{B4})$$

where N is the number of data. Equation (B3) is solved by least squares, and the resulting model prediction, \tilde{b}_i , is compared with the scaled data b_i to obtain one more scaling factor:

$$\beta = \exp\left(\frac{\sum_{j=1}^N \log \frac{b_i}{\tilde{b}_i}}{N}\right). \quad (\text{B5})$$

Our ‘best fit’ scaling constants are then obtained as:

$$A_i = \frac{\beta}{\alpha_i} C_i, \quad (\text{B6})$$

or with perturbations within the a priori bounds as:

$$A_i = \frac{\beta}{\alpha_i} C_i \exp(m_i), \quad (\text{B7})$$

where m_i is a random number drawn from the interval $[m_i^L, m_i^U]$.

[78] The randomization of the scaling constants after the above data fit is a key to an efficient MCMC simulation, and data fitting itself must also be done efficiently. If different creep mechanisms considered in a composite flow law do not occur independently, the flow law would not be linear in relevant scaling constants. In this case, randomizing the scaling constants may become more involved than considered here.

[79] **Acknowledgments.** This work was sponsored by the U.S. National Science Foundation under grant EAR-0449517 (JK). Shenghua Mei, Greg Hirth, Dave Kohlstedt, and Haemyeong Jung kindly provided details on experimental conditions. Official reviews by the Associate Editor Ernie Rutter, Georg Dresen, and an anonymous reviewer were helpful to improve the accuracy and clarity of the manuscript.

References

- Ave Lallemand, H. G., J.-C. C. Mercier, N. L. Carter, and J. V. Ross (1980), Rheology of the upper mantle: Inferences from peridotite xenoliths, *Tectonophysics*, **70**, 85–113.
- Bai, Q., S. J. Mackwell, and D. L. Kohlstedt (1991), High-temperature creep of olivine single crystals. 1. Mechanical results for buffered samples, *J. Geophys. Res.*, **96**, 2441–2463.
- Bell, D. R., G. R. Rossman, J. Maldener, D. Endisch, and F. Rauch (2003), Hydroxide in olivine: A quantitative determination of the absolute amount and calibration of the IR spectrum, *J. Geophys. Res.*, **108**(B2), 2105, doi:10.1029/2001JB000679.
- Billen, M. I., and G. Hirth (2005), Newtonian versus non-Newtonian upper mantle viscosity: Implications for subduction initiation, *Geophys. Res. Lett.*, **32**, L19304, doi:10.1029/2005GL023457.
- Braun, M. G., G. Hirth, and E. M. Parmentier (2000), The effects of deep damp melting on mantle flow and melt generation beneath mid-ocean ridges, *Earth Planet. Sci. Lett.*, **176**, 339–356.
- Bystricky, M., and S. Mackwell (2001), Creep of dry clinopyroxene aggregates, *J. Geophys. Res.*, **106**, 13,443–14,354.
- Chopra, P. N., and M. S. Paterson (1984), The role of water in the deformation of dunite, *J. Geophys. Res.*, **89**, 7861–7876.
- Deming, W. E. (1943), *Statistical Adjustment of Data*, John Wiley & Sons, New York.
- Franssen, R. C. M. W. (1994), The rheology of synthetic rocksalt in uniaxial compression, *Tectonophysics*, **233**, 1–40.

- Frenkel, D., and B. Smit (2002), *Understanding Molecular Simulation*, 2nd Ed., Academic Press, Boston.
- Gamerman, D. (1997), *Markov Chain Monte Carlo: Stochastic Simulation of Bayesian Inference*, CRC Press, New York.
- Gershenfeld, N. (1998), *The Nature of Mathematical Modeling*, Cambridge, New York.
- Geyer, C. J. (1992), Practical Markov chain Monte Carlo, *Statist. Sci.*, **7**, 473–483.
- Gilks, W. R., S. Richardson, and D. J. Spiegelhalter (1996), *Markov Chain Monte Carlo in Practice*, Chapman & Hall, New York.
- Goetze, C., and B. Evans (1979), Stress and temperature in the bending lithosphere as constrained by experimental rock mechanics, *Geophys. J. R. Astr. Soc.*, **59**, 463–478.
- Goldsby, D. L., and D. L. Kohlstedt (1997), Grain boundary sliding in fine-grained ice I, *Scripta Materialia*, **37**, 1399–1406.
- Goldsby, D. L., and D. L. Kohlstedt (2001), Superplastic deformation of ice: Experimental observations, *J. Geophys. Res.*, **106**, 11,017–11,030.
- Hager, B. H., and R. J. O’Connell (1981), A simple global model of plate dynamics and mantle convection, *J. Geophys. Res.*, **86**, 4843–4867.
- Hager, B. H., R. W. Clayton, M. A. Richards, R. P. Comer, and A. M. Dziewonski (1985), Lower mantle heterogeneity, dynamic topography and the geoid, *Nature*, **313**, 541–545.
- Hall, C. E., and E. M. Parmentier (2003), Influence of grain size evolution on convective instability, *Geochem. Geophys. Geosyst.*, **4**(3), 1029, doi:10.1029/2002GC000308.
- Hart, S. R., and A. Zindler (1986), In search of a bulk-Earth composition, *Chem. Geol.*, **57**, 247–267.
- Hirth, G., and D. L. Kohlstedt (1995a), Experimental constraints on the dynamics of the partially molten upper mantle: Deformation in the diffusion creep regime, *J. Geophys. Res.*, **100**, 1981–2001.
- Hirth, G., and D. L. Kohlstedt (1995b), Experimental constraints on the dynamics of the partially molten upper mantle: Deformation in the dislocation creep regime, *J. Geophys. Res.*, **100**, 15,441–15,449.
- Hirth, G., and D. L. Kohlstedt (1996), Water in the oceanic mantle: Implications for rheology, melt extraction, and the evolution of the lithosphere, *Earth Planet. Sci. Lett.*, **144**, 93–108.
- Hirth, G., and D. L. Kohlstedt (2003), Rheology of the upper mantle and the mantle wedge: A view from the experimentalists, in *Inside the Subduction Factory*, edited by J. Eiler, pp. 83–105, AGU, Washington, D.C.
- Jung, H., and S. Karato (2001), Effects of water on dynamically recrystallized grain-size of olivine, *J. Struct. Geol.*, **23**, 1337–1344.
- Jung, H., I. Katayama, Z. Jiang, T. Hiraga, and S. Karato (2006), Effect of water and stress on the lattice-preferred orientation of olivine, *Tectonophysics*, **421**, 1–22.
- Karato, S. (1986), Does partial melting reduce the creep strength of the upper mantle?, *Nature*, **319**, 309–310.
- Karato, S. (1989), Grain growth kinetics in olivine aggregates, *Tectonophysics*, **168**, 255–273.
- Karato, S. (2006), Influence of hydrogen-related defects on the electrical conductivity and plastic deformation of mantle minerals: A critical review, in *Earth’s Deep Water Cycle*, edited by S. Jacobsen and S. Lee van der, pp. 113–130, AGU, Washington D.C.
- Karato, S. (2007), *Deformation of Earth Materials: Introduction to the Rheology of the Solid Earth*, Cambridge Univ. Press, New York.
- Karato, S., and H. Jung (2003), Effects of pressure on high-temperature dislocation creep in olivine, *Philos. Mag.*, **83**, 401–414.
- Karato, S., and P. Wu (1993), Rheology of the upper mantle: A synthesis, *Science*, **260**, 771–778.
- Karato, S.-I., M. Paterson, and J. D. Fitzgerald (1986), Rheology of synthetic olivine aggregates: Influence of grain size and water, *J. Geophys. Res.*, **91**, 8151–8176.
- Kneller, E. A., P. E. van Keken, S. Karato, and J. Park (2005), B-type olivine fabric in the mantle wedge: Insights from high-resolution non-Newtonian subduction zone models, *Earth Planet. Sci. Lett.*, **231**, 781–797.
- Koga, K., E. Hauri, M. Hirschmann, and D. Bell (2003), Hydrogen concentration analysis using SIMS and FTIR: Comparison and calibration for nominally anhydrous minerals, *Geochem. Geophys. Geosyst.*, **4**(2), 1019, doi:10.1029/2002GC000378.
- Kohlstedt, D. L., H. Keppler, and D. C. Rubie (1996), Solubility of water in α , β and γ phases of $(\text{Mg, Fe})_2\text{SiO}_4$, *Comp. Mineral. Petrol.*, **123**, 345–357.
- Li, L., D. Weidner, P. Raterron, J. Chen, and M. Vaughan (2004), Stress measurements of deforming olivine at high pressure, *Phys. Earth Planet. Inter.*, **143–144**, 357–367.
- Liu, J. S. (2001), *Monte Carlo Strategies in Scientific Computing*, Springer, New York.
- Macdonald, J. R., and W. J. Thompson (1992), Least-squares fitting when both variables contain errors: Pitfalls and possibilities, *Am. J. Phys.*, **60**, 66–73.

- McDonnell, R. D., C. J. Peach, and C. J. Spiers (1999), Flow behavior of fine-grained synthetic dunite in the presence of 0.5 wt% of H₂O, *J. Geophys. Res.*, *104*, 17,823–17,845.
- McDonough, W. F., and S.-s. Sun (1995), The composition of the Earth, *Chem. Geol.*, *120*, 223–253.
- Mei, S., and D. L. Kohlstedt (2000a), Influence of water on plastic deformation of olivine aggregates, 1. Diffusion creep regime, *J. Geophys. Res.*, *105*, 21,457–21,469.
- Mei, S., and D. L. Kohlstedt (2000b), Influence of water on plastic deformation of olivine aggregates, 2. Dislocation creep regime, *J. Geophys. Res.*, *105*, 21,471–21,481.
- Metropolis, N., A. W. Rosenbluth, M. N. Rosenbluth, A. H. Teller, and E. Teller (1953), Equations of state calculations by fast computing machines, *J. Chem. Phys.*, *21*, 1087–1091.
- Mosegaard, K., and A. Tarantola (1995), Monte Carlo sampling of solutions to inverse problems, *J. Geophys. Res.*, *100*, 12,431–12,447.
- Nakada, M., and K. Lambeck (1989), Late Pleistocene and Holocene sea-level change in the Australian region and mantle rheology, *Geophys. J.*, *96*, 497–517.
- Parrish, D. K., and A. F. Gangi (1981), A nonlinear least squares technique for determining multip-mechanism, high-temperature creep flow laws, in *Mechanical Behavior of Crustal Rocks: The Handin Volume*, edited by N. L. Carter, M. Friedman, J. M. Logan, and D. W. Stearns, pp. 287–298, AGU, Washington, D.C.
- Paterson, M. S. (1982), The determination of hydroxyl by infrared absorption in quartz, silicate glasses and similar materials, *Bull. Mineral.*, *105*, 20–29.
- Poirier, J.-P., C. Sotin, and S. Beauchesne (1990), Experimental deformation and data processing, in *Deformation Processes in Minerals, Ceramics and Rocks*, edited by D. J. Barber and P. G. Meredith, pp. 179–189, Unwin Hyman, Boston.
- Press, W. H., S. A. Teukolsky, W. T. Vetterling, and B. P. Flannery (1992), *Numerical Recipes in C*, 2nd ed., Cambridge Univ. Press, New York.
- Reed, B. C. (1989), Linear least-squares fits with errors in both coordinates, *Am. J. Phys.*, *57*, 642–646.
- Renner, J., B. Stöckhert, A. Zerbian, K. Röller, and F. Rummel (2001), An experimental study into the rheology of synthetic polycrystalline coesite aggregates, *J. Geophys. Res.*, *106*, 19,411–19,429.
- Ricard, Y., and B. Wuming (1991), Inferring the mantle viscosity and its three dimensional structure from geoid, topography and plate velocities, *Geophys. J.*, *105*, 561–571.
- Robert, C. P., and G. Cassella (2004), *Monte Carlo Statistical Methods*, Springer, New York.
- Sambridge, M., and K. Mosegaard (2002), Monte Carlo methods in geophysical inverse problems, *Rev. Geophys.*, *40*(3), 1009, doi:10.1029/2000RG000089.
- Smith, A. F. M., and G. O. Roberts (1993), Bayesian computation via the Gibbs sampler and related Markov chain Monte Carlo methods, *J. R. Stat. Soc. B*, *55*, 3–23.
- Sotin, C., and J.-P. Poirier (1984), Analysis of high temperature creep experiments by generalized non-linear inversion, *Mech. Mat.*, *3*, 311–317.
- Takei, Y., and B. K. Holtzman (2006), Viscous constitutive relations of partially molten rocks in terms of grain-boundary contiguity, *Eos Trans. AGU*, *87*(52), Fall Meet. Supp.
- Tarantola, A. (1987), *Inverse Problem Theory: Methods for Data Fitting and Model Parameter Estimation*, Elsevier, New York.
- Tarantola, A., and B. Valette (1982a), Inverse problems: Quest of information, *J. Geophys.*, *50*, 159–170.
- Tarantola, A., and B. Valette (1982b), Generalized nonlinear inverse problems solved using the least squares criterion, *Rev. Geophys.*, *20*, 219–232.
- von Neumann, J. (1951), Various techniques used in connection with random digits, *Nat. Bur. Stand. Appl. Math. Ser.*, *12*, 36–38.
- Weertman, J. (1970), The creep strength of the Earth's mantle, *Rev. Geophys.*, *8*, 146–168.
- Wu, P., and W. Peltier (1983), Glacial isostatic adjustment and the free air gravity anomaly as a constraint on deep mantle viscosity, *Geophys. J. R. Astron. Soc.*, *74*, 377–449.
- Zhang, S., S. Karato, J. Fitz Gerald, U. H. Faul, and Y. Zhou (2000), Simple shear deformation of olivine aggregates, *Tectonophysics*, *316*, 133–152.
- Zhao, Y.-H., S. B. Ginsberg, and D. L. Kohlstedt (2004), Solubility of hydrogen in olivine: Dependence on temperature and iron content, *Comp. Mineral. Petrol.*, *147*, 155–161.

S.-I. Karato and J. Korenaga, Department of Geology and Geophysics, Yale University, P.O. Box, 208109, New Haven, CT 06520-8109, USA. (shun-ichiro.karato@yale.edu; jun.korenaga@yale.edu)